Two approaches to compute unsteady compressible two-phase flow models with stiff relaxation terms

Jean-Marc Hérard, Guillaume Jomée

Two approaches to compute unsteady compressible two-phase flow models with stiff relaxation terms

Jean-Marc Hérard (1,2), Guillaume Jomée (1,2)

(1) EDF Lab Chatou, 6 quai Watier, 78400, Chatou, France
(2) Institut de Mathématiques de Marseille, Technopôle Château-Gombert 39, rue Frédéric Joliot-Curie 13453 Marseille Cedex 13, France

Abstract

The paper deals with the numerical modeling of two-phase flows while using Baer-Nunziato type models. Focus is given here on the numerical treatment of source terms that involve three (or four) relaxation time scales. A new coupled approach relying on the continuous analysis of the system of ODEs is compared with a more widely used strategy grounded on the fractional step approach. Properties of schemes are given in both cases. Several numerical applications show that the coupled approach should be preferred for both stability and accuracy reasons.

Introduction

Many industrial studies urge the development of suitable models and reliable numerical tools, in order to predict two-phase or even multiphase flows. While restricting to two-phase flows, at least two different modelling strategies may be considered.

A first one basically assumes that inner processes involving various relaxation time scales are such that a full instantaneous equilibrium is reached everywhere in the flow. This has led to a rather broad class of so-called homogeneous two-phase flow models, among which we may at least cite [1, 4, 22, 47, 39].

When very fast transients are at stake or when droplet atomization occurs, a second strategy, which is grounded on full disequilibrium models, may be retained. The present contribution clearly lies within this framework. More precisely, focus will be given on a class of two-phase flow models that is now well-known,see [3, 60, 15, 13, 26, 32, 48, 55, 29, 30, 38] among others. It must be recalled that three (respectively four) relaxation time scales are embedded in these gas-liquid (respectively liquid-vapour, thus including mass transfer) flow models. The latter time scales obviously require suitable closure laws, that can be found in the literature, see [28, 7, 8, 4, 19, 46, 54] among others. These relaxation time scales may be quite distinct and may depend on the application. Assumptions regarding some relaxation time scales may lead to relaxation models such as [24, 51, 23, 34] among others. In the present work, no hypothesis concerning the relaxation time scales is retained, in order to preserve the widest range of applications.

Moreover, the dynamics of the underlying relaxation process in Baer-Nunziato type models has not been thoroughly studied yet. This question is often (implicitly) addressed by seeing the total entropy as a Lyapunov function. In the homogeneous case, *i.e.* without convective terms, that ensures the stability close to the steady state, or equivalently here, close to the mechanical and thermodynamic equilibrium between the two-phases. However, in many cases, such as vapour explosion or loss-of-coolant accidents, the initial conditions may be set far from thermodynamic equilibrium. Thus, a better understanding of the effective relaxation process is crucial, in order to guarantee the return to equilibrium. In this paper, conditions of effective relaxation are exhibited and discussed for various equations of state (EOS).

Up to now, most of the numerical strategies that have been proposed in order to obtain approximate solutions of these non-equilibrium two-phase flow models, are grounded on the use of a two-step algorithm. The latter includes:

(i) an **explicit evolution step** that treats all convective contributions together with help of Riemann solvers, relaxation solvers or Discontinuous Galerkin methods, see for example [15, 26, 59, 61, 62, 64, 2, 14, 17, 35, 55, 58], and

(ii) an **implicit step that deals with source terms** associated with the former relaxation time scales, as in [2, 17, 18, 25, 26, 35, 36, 52, 53, 55, 58] among others.

It seems worth emphasizing that, in the framework of immiscible three-phase flow models, such as those proposed in [40], the problem of the preservation of admissible states through the convective subsystem (step (i)) has been addressed in section 2.2.4 of [6], while focusing on simple Stiffened Gas EOS. This result obviously applies in the framework of two-phase flow models considered here. The first explicit step (i) introduces some constraint on the time step for obvious stability issues. This, in turn, renders the implicit treatment of step (ii) mandatory.

Concerning the second implicit step (ii), a fractional step approach has been widely applied up to now, that treats separately the distinct relaxation time scales, see [17, 25, 55, 18, 2, 35] among others. In addition, the numerical treatment of the source terms, using strong hypothesis on some relaxation time scales, has been investigated in the literature, see for example [53, 52, 36]. However, the fractional step approach used for handling the source terms may suffer from deficiencies, and even lead to a blow-up of the code in some extreme situations, see for example [6] which tackles the problem of vapour explosion. Hence, this motivates to investigate further on the set of coupled ODEs accounting for source terms, and meanwhile derive relevant and more coupled schemes in order to tackle extreme situations. In the present work, a new robust numerical scheme without any assumption on the relaxation time scales is presented.

In the following, emphasis is given on the stability of the scheme. We will also examine whether the accuracy of the new scheme is improved, or not, on a given mesh size, by comparing it with the fractional step approach.

The paper is organised as follows. The governing set of equations is recalled first, and the main properties of the model are given. A few results are then provided and discussed, which concern the true inner relaxation process with respect to temperature, pressure, and velocity in gas-liquid flow models. Afterwards, two distinct algorithms will be considered. The first one is classical. It takes the three (respectively four) relaxation effects into account in a fractional step approach involving three steps when dealing with gas-liquid flows (respectively four in the case of liquid-vapour flows). The second one relies on the investigation of coupled relaxation effects, as discussed in section 1. Some important properties of the latter schemes are detailed. Both schemes are tested against Chauvin experiment, and a more complex situation arising from the vapour explosion framework. As expected, the comparison of the two schemes is clearly in favour of the coupled algorithm. **Appendices** complete the paper. In particular, **Appendix** 7 discusses the influence of the ratio of pressure and thermal relaxation time scales, whereas **Appendix** 8 highlights the influence of the interfacial area.

1 Governing equations of the two-phase flow model and main properties

We first introduce the set of governing equations of the two-phase flow models examined in the sequel. These include the mass balance equations, the momentum and energy balance equations, together with the evolution of the statistical fractions. We also refer the reader to some companion references [3, 13, 25, 27, 29, 30, 32, 37, 34, 48, 38, 55, 60] that may help and provide additional details.

Both gas-liquid flows (without any mass transfer), and liquid-vapour flows, which involve a unique component (basically water in our framework), will be examined in the sequel. Thus, we introduce rather logical notations as follows.

The statistical fractions of the immiscible liquid phase and the gas/vapour phase are noted $\alpha_l(x,t)$ and $\alpha_{g,v}(x,t)$(for gas and vapour respectively). They are such that:

$$\alpha_l(x,t) + \alpha_{g,v}(x,t) = 1 \tag{1}$$

In order to ease notations, we will favour the liquid phase (indexed by l) in both cases. All variables in the gas (respectively the vapour) phase will be indexed by g (respectively by v).

Within the $k-$phase, and for $k \in (l,g)$ or $k \in (l,v)$, U_k, P_k, ρ_k, $m_k = \alpha_k \rho_k$ and E_k will respectively denote the phasic mean velocity, mean pressure, mean density, mass fraction and mean total energy, setting:

$$E_k = \rho_k(\epsilon_k(\rho_k, P_k) + U_k^2/2) \tag{2}$$

where $\epsilon_k(\rho_k, P_k)$ denotes the internal energy within phase k. The gas-liquid state variable W^{lg} will be noted:

$$W^{lg} = (\alpha_l, m_l, m_g, m_l U_l, m_g U_g, \alpha_l E_l, \alpha_g E_g) \tag{3}$$

while the liquid-vapour state variable will correspond to:

$$W^{lv} = (\alpha_l, m_l, m_v, m_l U_l, m_v U_v, \alpha_l E_l, \alpha_v E_v) \tag{4}$$

In the sequel, in order to ease notations, the state variable is called W; W can refer to W^{lg} or W^{lv}, depending on the current treated case. If no precision is given, then the results stand true for both cases.

1.1 Open set of equations

We may now write the governing set of PDE, which correspond to balance equations for mass, momentum and energy, within phase k, and for the statistical fraction α_l. These are:

$$\begin{cases} \partial_t(\alpha_l) + \mathscr{V}_I(W)\nabla\alpha_l = \phi_l(W) \ ; \\ \partial_t(m_k) + \nabla\cdot(m_k U_k) = \Gamma_k(W) \ ; \\ \partial_t(m_k U_k) + \nabla\cdot(m_k U_k \times U_k + \alpha_k P_k \mathscr{I}) - \Pi_I(W)\nabla\alpha_k = S_{Q_k}(W) \ ; \\ \partial_t(\alpha_k E_k) + \nabla\cdot(\alpha_k U_k(E_k + P_k)) + \Pi_I(W)\partial_t(\alpha_k) = S_{E_k}(W) \ . \end{cases} \tag{5}$$

for $k \in (l,g)$, or $k \in (l,v)$.
When focusing on gas-liquid flows, we obviously have:

$$\Gamma_l(W) = \Gamma_g(W) = 0 \ , \tag{6}$$

whereas for liquid-vapour flows, the following constraint holds:

$$\Gamma_l(W) + \Gamma_v(W) = 0 \ . \tag{7}$$

For $k \in (l,g)$, or $k \in (l,v)$, interfacial transfer terms arising in momentum and energy balance equations, comply with:

$$\sum_k S_{E_k}(W) = 0 \tag{8}$$

together with:

$$\sum_k S_{Q_k}(W) = 0 \tag{9}$$

1.2 Entropy-consistent closure laws

We assume that the interfacial velocity $\mathscr{V}_I(W)$ takes the form:

$$\mathscr{V}_I(W) = \beta(W)U_l + (1-\beta(W))U_{v,g} \tag{10}$$

with $\beta(W) \in [0,1]$. Hence, it satisfies Galilean invariance. We will specify later on some scalar functions $\beta(W)$ that will guarantee unique field by field jump conditions (see also the reference paper [13]). The next definitions require introducing phasic entropies $S_k(\rho_k, P_k)$ and temperatures $T_k(\rho_k, P_k)$, which are such that:

$$c_k^2 \partial_{P_k}(S_k(\rho_k, P_k)) + \partial_{\rho_k}(S_k(\rho_k, P_k)) = 0 \ , \tag{11}$$

where:

$$\rho_k c_k^2 = (\frac{P_k}{\rho_k} - \rho_k \partial_{\rho_k} (\epsilon_k(\rho_k, P_k)))/(\partial_{P_k} (\epsilon_k(\rho_k, P_k))) \tag{12}$$

and:

$$\frac{1}{T_k} = \frac{\partial_{P_k} (S_k(\rho_k, P_k))}{\partial_{P_k} (\epsilon_k(\rho_k, P_k))} \ . \tag{13}$$

Using the latter definitions, we get the admissible interfacial pressure $\Pi_I(W)$ as:

$$\Pi_I(W) = \chi(W) P_l + (1 - \chi(W)) P_{v,g} \tag{14}$$

where the function $\chi(W)$ is obtained straightforwardly:

$$\chi(W) = \frac{(1 - \beta(W)) T_{v,g}}{(1 - \beta(W)) T_{v,g} + \beta(W) T_l} \tag{15}$$

We emphasize that this enables to recover the standard Baer-Nunziato closure $\Pi_I(W) = P_l, \mathscr{V}_I(W) = U_{g,v}$. It also guarantees the Realisable Interfacial Pressure condition (see appendix 7 and [43]). We recall now some classical results.

Property 1: (Structure of the one-dimensional convective subset)
We restrict to the one-dimensional framework. We have the following results:

- *The homogeneous convective part (left-hand side) of system (5) is hyperbolic. The seven real eigenvalues read:*

$$\begin{gathered} \lambda_0(W) = \mathscr{V}_I(W) \ ; \\ \lambda_1(W) = U_l - c_l \quad ; \quad \lambda_2(W) = U_l \quad ; \quad \lambda_3(W) = U_l + c_l \ ; \\ \lambda_4(W) = U_{v,g} - c_{v,g} \quad ; \quad \lambda_5(W) = U_{v,g} \quad ; \quad \lambda_6(W) = U_{v,g} + c_{v,g} \ . \end{gathered} \tag{16}$$

  Right eigenvectors span the whole space away from the resonance state:

$$|U_k - \mathscr{V}_I(W)| = c_k \tag{17}$$

- *For $k \in (l, v)$ or $k \in (l, g)$, waves associated with eigenvalues $U_k \pm c_k$ are Genuinely Non-Linear, and waves associated with eigenvalues U_k are Linearly Degenerate.*

- *The coupling wave associated with $\lambda_0(W)$ is Linearly Degenerate if:*

$$\beta(W)(1 - \beta(W)) = 0 \tag{18}$$

  or if:

$$\beta(W) = \frac{m_l}{m_l + m_{v,g}} \ . \tag{19}$$

- *System (5) can be symmetrized away from resonant states (17).*

□

The proof of the first three points can be found in [13], while the fourth one is available in [16]. Moreover, details pertaining to Riemann invariants within fields associated with eigenvalues λ_{1-6} can also be found in the latter references. Even more, explicit analytic forms of Riemann invariants in the coupling wave can be found in the particular case $\beta(W) = 0$ in [20] and [13]. Owing to the LD structure of the coupling wave, when $\beta(W)$ is chosen in a suitable way, unique jump conditions may be defined in GNL fields for system (5). This was pointed out in [13], and a direct consequence is that the computation of shocks is meaningful in that case, since non-conservative products are well-defined in shock waves (in the non-resonant case): convergent approximations of shocks are not scheme dependent (see [35]).

Now, coming back to the three-dimensional setting, we introduce the entropy - entropy flux pair (η, F_η):

$$\eta = \sum_k m_k S_k(\rho_k, P_k), \qquad \mathscr{F}_\eta = \sum_k m_k S_k(\rho_k, P_k) U_k, \tag{20}$$

Considering smooth solutions, we can examine the time evolution of η in system (5). Straightforward calculations enable to get:

$$\partial_t(\eta) + \nabla \cdot (\mathscr{F}_\eta) = RHS_\eta(W) \ . \tag{21}$$

with an explicit form of the right-hand side $RHS_\eta(W)$ depending on the closure laws for $\phi_l(W)$, $\Gamma_l(W)$, $S_{Q_k}(W)$ and $S_{E_k}(W)$.

In order to ease the presentation and calculations, we rewrite source terms in a slightly different form and define translated unknowns $D_k(W)$ and $\psi_k(W)$ such that:

$$\left\{ \begin{array}{l} D_k(W) = S_{Q_k}(W) - \dfrac{U_l + U_{v,g}}{2}\Gamma_k(W) \ ; \\ \psi_k(W) = S_{E_k}(W) - V_I^E(W) D_k(W) - \dfrac{U_l U_{v,g}}{2}\Gamma_k(W) \ ; \end{array} \right. \tag{22}$$

Taking interfacial constraints on $S_{Q_k}(W)$ and $S_{E_k}(W)$ into account, we must fulfil:

$$D_l(W) + D_{v,g}(W) = 0 \ , \tag{23}$$

and also:

$$\psi_l(W) + \psi_{v,g}(W) = 0 \ . \tag{24}$$

We consider a consistent and Galilean invariant formulation for $V_I^E(W)$, hence:

$$V_I^E(W) = \beta^E(W) U_l + (1 - \beta^E(W)) U_{v,g} \ . \tag{25}$$

where $\beta^E(W)$ must lie in $[0, 1]$. We classically note in the sequel:

$$\mu_k = h_k - T_k S_k \tag{26}$$

where the free enthalpy h_k writes:

$$h_k = \epsilon_k(\rho_k, P_k) + \frac{P_k}{\rho_k} \tag{27}$$

Eventually, considering the notations:

$$\left\{ \begin{array}{l} \Delta P = P_l - P_{v,g} \ , \\ \Delta U = U_l - U_{v,g} \ , \\ \Delta T = T_l - T_{v,g} \ , \\ \Delta \mu = \dfrac{\mu_l}{T_l} - \dfrac{\mu_{v,g}}{T_{v,g}} \ , \end{array} \right. \tag{28}$$

we obtain the following classical result ([3, 26, 49, 18, 38, 55]):

Property 2: (Entropy consistent source terms for a class of two-phase flow models)
We consider the following source terms:

$$\left\{ \begin{array}{l} \phi_l(W) = K(W)\Delta P \ , \\ D_l(W) = -d(W)\Delta U \ , \\ \psi_l(W) = -q(W)\Delta T \ , \\ \Gamma_l(W) = -\Lambda(W)\Delta \mu \ , \end{array} \right. \tag{29}$$

Then smooth solutions of system (5) *agree with:*

$$\partial_t(\eta) + \nabla . (\mathscr{F}_\eta) = RHS_\eta(W) \geqslant 0 \tag{30}$$

providing positive functions $K(W), d(W), q(W), \Lambda(W)$.

□

Proof. :

The proof is simple. The right-hand side term RHS_η is simply:

$$\begin{aligned} RHS_\eta = & \frac{1}{T_l T_{v,g}} \psi_l(W) \left(T_{v,g} - T_l\right) \\ & + \left(\frac{1-\beta^E(W)}{T_l} + \frac{\beta^E(W)}{T_{v,g}} \right) D_l(W)(U_{v,g} - U_l) \\ & + \left(\frac{1-\chi(W)}{T_l} + \frac{\chi(W)}{T_{v,g}} \right) \phi_l(W)(P_l - P_{v,g}) \\ & + (\frac{\mu_{v,g}}{T_{v,g}} - \frac{\mu_l}{T_l}) \Gamma_l(W) \end{aligned} \tag{31}$$

and thus positive, owing to (29). □

Note that the second, third and fourth closure laws arising in (29) are also entropy-consistent when focusing on single-pressure two-fluid six-equation models ([46]). Closure laws for heat transfer and drag coefficients arising in $q(W)$ and $d(W)$ can be taken from the standard literature (see [46] among others). Besides, references [28, 7, 8, 44] provide closure laws for the pressure relaxation time scales $\tau_P(W)$ involved in $K(W)$.

1.3 Relaxation process in a class of two-phase flow models [1]

When focusing on gas-liquid flows, where no mass transfer occurs, a straightforward question arises, which concerns the (physically expected) decay of velocity, pressure and temperature gaps. Note that this problem has been investigated recently in [43], while focusing on the *sole* pressure gaps, though examining several two-phase or multiphase flow models. While restricting to the present class of gas-liquid two-phase flow models, the problem at stake here is whether the whole relaxation process is active for the three quantities ΔP, ΔU and ΔT. For that purpose, we consider some homogeneous situation with no gradient of mean variables, thus considering an initial condition for system (5), such that:

$$\nabla \psi(x, t=0) = 0 \tag{33}$$

whatever ψ stands for. Hence, system (5) reduces to:

$$\left\{ \begin{array}{l} \partial_t\left(\alpha_l\right) = \phi_l(W) \ ; \\ \partial_t\left(m_k\right) = 0 \ ; \\ \partial_t\left(m_k U_k\right) = S_{Q_k}(W) \ ; \\ \partial_t\left(\alpha_k E_k\right) + \Pi_I(W) \partial_t\left(\alpha_k\right) = S_{E_k}(W) \ , \end{array} \right. \tag{34}$$

for $k \in (l, g)$. This system may be rewritten in a slightly different form:

$$\left\{ \begin{array}{l} \partial_t\left(\alpha_l\right) = \phi_l(W) \ ; \\ \partial_t\left(\alpha_l E_l\right) + \Pi_I(W) \partial_t\left(\alpha_l\right) = S_{E_l}(W) \ ; \\ \partial_t\left(m_l U_l\right) = S_{Q_l}(W) \ ; \\ \partial_t\left(m_l\right) = \partial_t\left(m_g\right) = 0 \ ; \\ \partial_t\left(m_l U_l + m_g U_g\right) = 0 \ ; \\ \partial_t\left(\alpha_l E_l + \alpha_g E_g\right) = 0 \ . \end{array} \right. \tag{35}$$

Equipped with this system (34), we may write the governing equations for the three quantities ΔP, ΔU and ΔT.

[1] Consider the vector Δ defined at each point (x,t), the components of which are quantity discrepancies between phases, corresponding to states that make the source terms vanish. If the solution of the governing equations, without any convective term, complies with:

$$\partial_t\left(\|\Delta\|_{L^2}\right) \leqslant 0 \tag{32}$$

then the relaxation process is said to be effective.

If we note:

$$\Delta^{lg} = (\Delta U, \Delta T, \Delta P)^T \tag{36}$$

simple calculations enable to get:

$$\partial_t \left(\Delta^{lg}\right) = -\mathscr{R}^{lg}(W)\Delta^{lg} \tag{37}$$

where the matrix $\mathscr{R}^{lg}(W) \in \mathscr{M}_3(\mathbb{R})$ is given by:

$$\mathscr{R}^{lg}(W) = \begin{pmatrix} a^{lg}_{UU}(W) & 0 & 0 \\ a^{lg}_{TU}(W) & a^{lg}_{TT}(W) & a^{lg}_{TP}(W) \\ a^{lg}_{PU}(W) & a^{lg}_{PT}(W) & a^{lg}_{PP}(W) \end{pmatrix} \tag{38}$$

Coefficients in matrix $\mathscr{R}^{lg}(W)$ read:

$$a^{lg}_{UU}(W) = d(W)\left(\frac{1}{m_l} + \frac{1}{m_g}\right) , \tag{39}$$

together with [2]:

$$\begin{cases} a^{lg}_{TU}(W) = d(W)\Delta U \left(\dfrac{\beta^E(W) - 1}{m_l \partial_{T_l}(\epsilon_l)|_{\rho_l}} + \dfrac{\beta^E(W)}{m_g \partial_{T_g}(\epsilon_g)|_{\rho_g}}\right) , \\ a^{lg}_{TT}(W) = q(W)\left(\dfrac{1}{m_l \partial_{T_l}(\epsilon_l)|_{\rho_l}} + \dfrac{1}{m_g \partial_{T_g}(\epsilon_g)|_{\rho_g}}\right) , \\ a^{lg}_{TP}(W) = K(W)\left(\dfrac{\Pi_I - \rho_l^2 \partial_{\rho_l}(\epsilon_l)|_{T_l}}{m_l \partial_{T_l}(\epsilon_l)|_{\rho_l}} + \dfrac{\Pi_I - \rho_g^2 \partial_{\rho_g}(\epsilon_g)|_{T_g}}{m_g \partial_{T_g}(\epsilon_g)|_{\rho_g}}\right) , \end{cases} \tag{40}$$

and:

$$\begin{cases} a^{lg}_{PU}(W) = d(W)\Delta\mathscr{U} \left(\dfrac{\beta^E(W) - 1}{m_l \partial_{P_l}(\epsilon_l)|_{\rho_l}} + \dfrac{\beta^E(W)}{m_g \partial_{P_g}(\epsilon_g)|_{\rho_g}}\right) , \\ a^{lg}_{PT}(W) = q(W)\left(\dfrac{1}{m_l \partial_{P_l}(\epsilon_l)|_{\rho_l}} + \dfrac{1}{m_g \partial_{P_g}(\epsilon_g)|_{\rho_g}}\right) , \\ a^{lg}_{PP}(W) = K(W)\left(A_l + A_g + (\dfrac{\chi(W) - 1}{m_l \partial_{P_l}(\epsilon_l)|_{\rho_l}} + \dfrac{\chi(W)}{m_g \partial_{P_g}(\epsilon_g)|_{\rho_g}})\Delta P\right) . \end{cases} \tag{41}$$

We have used the following notation here for $k = l, g$:

$$A_k = \frac{\rho_k c_k^2}{\alpha_k} \tag{42}$$

Thus, we get:

Property 3: (Relaxation effects in a class of gas-liquid flow models)
We assume that equations of state within each phase are such that, for $k = l, g$:

$$0 \leqslant \partial_{T_k}(\epsilon_k)|_{\rho_k} \tag{43}$$

Considering positive functions $K(W)$, $q(W)$, $d(W)$, the relaxation process is guaranteed for solutions of (34), if eigenvalues of matrix $\mathscr{R}^{lg}(W)$ are real and positive, or if they are complex with a positive real part. This is guaranteed if the pressure gap ΔP is sufficiently small in the following sense:

$$(P_g - P_l)\left(\frac{(\chi(W) - 1)\alpha_g}{\rho_l \partial_{P_l}(\epsilon_l)|_{\rho_l}} + \frac{\chi(W)\alpha_l}{\rho_g \partial_{P_g}(\epsilon_g)|_{\rho_g}}\right) \leqslant \alpha_g \rho_l c_l^2 + \alpha_l \rho_g c_g^2 , \tag{44}$$

and if the following condition holds:

$$\frac{a^{lg}_{TT}(W)a^{lg}_{PP}(W) - a^{lg}_{TP}(W)a^{lg}_{PT}(W)}{q(W)K(W)} > 0 . \tag{45}$$

□

[2] Considering the internal energies ϵ_k, with some abuse of notation, we will note in the sequel every change of variable of the functions $\epsilon_k(P_k, T_k) = \hat{\epsilon_k}(\rho_k, S_k) = \tilde{\epsilon_k}(\rho_k, P_k) = \mathring{\epsilon_k}(P_k, S_k) = \ddot{\epsilon_k}(\rho_k, T_k)$ as $\epsilon_k(P_k, T_k) = \epsilon_k(\rho_k, S_k) = \epsilon_k(\rho_k, P_k) = \epsilon_k(P_k, S_k) = \epsilon_k(\rho_k, T_k)$.

Proof. :

The proof is simple and can be found in [42]. We briefly recall it below.

- First, note that $\lambda = a^{lg}_{UU}(W)$ is an obvious real eigenvalue of matrix $\mathscr{R}^{lg}(W)$, and is positive.
- The remaining two eigenvalues of $\mathscr{R}^{lg}(W)$ are the two solutions $\lambda_\pm$ of the second-order polynomial:

$$p(\lambda) = \lambda^2 - (a^{lg}_{TT}(W) + a^{lg}_{PP}(W))\lambda + a^{lg}_{TT}(W)a^{lg}_{PP}(W) - a^{lg}_{TP}(W)a^{lg}_{PT}(W) \tag{46}$$

  Owing to conditions (43) and (44), the sum $a^{lg}_{TT}(W) + a^{lg}_{PP}(W)$ is positive, thus:

  - In case of complex eigenvalues, these are complex conjugate, and their real part a is equal to $(a^{lg}_{TT}(W) + a^{lg}_{PP}(W))/2$, thus positive ;
  - If the two eigenvalues $\lambda_\pm$ are real, we have: $\lambda_+ + \lambda_- = a^{lg}_{TT}(W) + a^{lg}_{PP}(W)$, thus the sum is positive. Moreover, the product $\lambda_+\lambda_-$ is equal to:

$$a^{lg}_{TT}(W)a^{lg}_{PP}(W) - a^{lg}_{TP}(W)a^{lg}_{PT}(W) \tag{47}$$

    and we can conclude that both λ_+ and λ_- are positive, owing to (45).

□

For sake of clarity, conditions (43), (44) and (45) are specified and discussed below for various EOS.

To do so, we consider the specific case **used in the sequel** which is: $\chi(W) = 0$ and thus $\Pi_I = P_g$.

- First, we note that condition (43) stands true in most EOS as it corresponds to a specific capacity at constant volume, which is expected to be positive.
- For a mixture of perfect gases:

$$P_k = \rho_k(\gamma_k - 1)\epsilon_k \tag{48}$$

  Conditions (44) and (45) always hold true, whatever the state variable W is.
- For a mixture of Stiffened-Gases we have:

$$\begin{cases} P_k + \gamma_k\hat{\Pi}_k = \rho_k(\gamma_k - 1)(\epsilon_k - \epsilon_{k_0}) \\ C_{v_k}T_k = \epsilon_k - \epsilon_{k_0} - \dfrac{\hat{\Pi}_k}{\rho_k} \end{cases} \tag{49}$$

  where $\gamma_k > 1$, $\hat{\Pi}_k > 0$ and ϵ_{k_0} are constants. Admissible states are such that: $P_k + \hat{\Pi}_k > 0$ and $\epsilon_k - \epsilon_{k_0} > 0$.

  Close to thermodynamic equilibrium, (44) is obviously satisfied. Condition (44) may be rewritten as:

$$\alpha_g(P_l + \hat{\Pi}_l) + (\alpha_l\gamma_g + \alpha_g(\gamma_l - 1))\,(P_g + \hat{\Pi}_g) + \alpha_g(\gamma_l - 1)(\hat{\Pi}_l - \hat{\Pi}_g) > 0 \tag{50}$$

  Equation (50) shows that, if $\hat{\Pi}_l > \hat{\Pi}_g$, condition (44) holds true, even **far** from thermodynamic equilibrium, in the admissible range: $P_k + \hat{\Pi}_k > 0$, $k \in \{l, g\}$.

  Condition (45) is equivalent to:

$$(m_lC_{v_l} + m_gC_{v_g})\left[\frac{\rho_l c_l^2}{\alpha_l\gamma_l} + \frac{\rho_g c_g^2}{\alpha_g\gamma_g}\right] \geqslant \left(\hat{\Pi}_l - \hat{\Pi}_g\right)\left[\frac{\hat{\Pi}_g - \hat{\Pi}_l}{T_g} + \frac{P_g}{T_g} - \frac{P_l}{T_l} + \frac{\hat{\Pi}_l(T_l - T_g)}{T_lT_g}\right] \tag{51}$$

  It must be emphasized that, **close to** the thermodynamic equilibrium, the right-hand side of (51) behaves as $-(\hat{\Pi}_l - \hat{\Pi}_g)^2/T_g$, and thus condition (45) is satisfied. This is an expected property as the entropy may be understood as a Lyapunov function of our system, owing to the closure of source terms (see property 2). Condition (51) -and thus (45)-, **no longer holds**, for any admissible state W, **far** from equilibrium.

- For a mixture of Noble-Abel Stiffened-Gases [50] we have:

$$\left\{ \begin{array}{l} P_k + \gamma_k \tilde{\Pi}_k = \dfrac{\rho_k(\gamma_k - 1)}{1 - \rho_k b_k}(\epsilon_k - \tilde{\epsilon}_{k_0}) \\ C_{v_k} T_k = \epsilon_k - \tilde{\epsilon}_{k_0} - \dfrac{(1 - \rho_k b_k)\tilde{\Pi}_k}{\rho_k} \end{array} \right. \tag{52}$$

  where $\gamma_k > 1$, $\tilde{\Pi}_k > 0$, $b_k > 0$ and $\tilde{\epsilon}_{k_0}$ are constants. Admissible states are such that: $P_k + \tilde{\Pi}_k > 0$, $(1 - \rho_k b_k) > 0$ and $\epsilon_k - \tilde{\epsilon}_{k_0} > 0$.

  Condition (44) writes as:

$$(\gamma_l - 1)(P_l - P_g) < (1 - \rho_l b_l)\left(\rho_l c_l^2 + \frac{\alpha_l}{\alpha_g}\rho_g c_g^2\right) \tag{53}$$

  Condition (45) is identical to the one exhibited for a mixture of Stiffened Gases (51).

In practice, for complex EOS, conditions (44) and (45) have to be checked in computer codes, in particular **far** from the thermodynamic equilibrium.

Remark 1:

- We may also note that the threshold effect on ΔP arising in condition (44) has already been pointed out in [6]. It arises when taking energy balance into account, and it does not exist when restricting to the barotropic case (see [41]). Its counterpart in the framework of immiscible three-phase flows and miscible two-phase flows is discussed in [43]. Straightforward numerical applications show that it can be hardly violated in practice. Thus, the latter constraint is indeed very weak. Actually, we may note that a simpler sufficient condition guarantees that it holds, whatever the values of statistical fractions are, which is:

$$|\Delta P|(|\frac{1}{\rho_l \partial_{P_l}(\epsilon_l)|_{\rho_l}}| + |\frac{1}{\rho_g \partial_{P_g}(\epsilon_g)|_{\rho_g}}|) \leqslant min(\rho_l c_l^2, \rho_g c_g^2) \tag{54}$$

- Moreover, a glance at the precise form of condition (45) shows that the relative amplitudes of time scales $\tau_P(W)$ and $\tau_T(W)$ respectively involved in closure laws of $K(W)$ and $q(W)$ have no impact on the latter condition.

- When accounting for mass transfer terms arising in liquid-vapour flow models, some additional constraints may arise, as emphasized in [42].

□

1.4 Relaxation time scales: τ_P, τ_T, τ_m and τ_U

In order to close system (5), the functions $q(W)$, $K(W)$, $\Lambda(W)$ and $d(W)$ are to be given and thus, four positive relaxation time scales τ_P, τ_T, τ_m and τ_U must be introduced.

- Pressure relaxation coefficient:

$$K(W) = \frac{\alpha_l \alpha_{g,v}}{\tau_P \mathscr{P}_0} \tag{55}$$

  with $\mathscr{P}_0$ a positive reference pressure.

- Heat transfer relaxation coefficient:

$$q(W) = \frac{m_l C_{v_l} m_g C_{v_{g,v}}}{\tau_T (m_l C_{v_l} + m_{g,v} C_{v_{g,v}})} \tag{56}$$

- Mass transfer relaxation coefficient :

$$\Lambda(W) = \frac{m_l m_v}{\tau_m (m_l + m_v)\Gamma_0} \tag{57}$$

with Γ_0 a positive reference fraction of $\dfrac{\mu}{T}$.

- Drag relaxation coefficient:

$$d(W) = \frac{m_l m_{g,v}}{\tau_U (m_l + m_{g,v})} \tag{58}$$

Different forms of τ_P, τ_T, τ_m and τ_U arise from the literature ([46], [28], [7], [8], [54],[4], [19]). Some of them will be detailed in the following sections.

2 Finite volume techniques to compute system (5)

We restrict herein to the computation of unsteady two-phase flows, while applying the two-fluid approach, and considering (5). Before going further on, we rewrite in a quite formal way system (5) as follows:

$$\partial_t (W) + \nabla \cdot (F(W)) + C(W)\nabla \alpha_l = S(W) \tag{59}$$

where W denotes the so-called conservative variable introduced in (3) or (4). Thus, $F(W)$ denotes the conservative flux accounting for convective effects, while $C(W)$ collects non-conservative contributions arising from the left-hand side of (5). Eventually, $S(W)$ accounts for the right-hand side source terms in (5).

We emphasize that, in the sequel, we assume that shock relations are uniquely defined in model (5), and thus we will restrict for our applications to closure laws for the interfacial velocity $\mathscr{V}_I(W)$ detailed in Property 1, or other suitable laws that comply with the LD structure of the coupling wave $\lambda_0(W) = \mathscr{V}_I(W)$. Of course, this provides a suitable framework in order to verify algorithms (while computing the error), when shocks occur in the flow.

Due to specific applications including water-hammer, loss of coolant accidents, steam explosion and other extreme situations including shock structures and high energy transfers between fluids or phases, robust algorithms are required, and for that purpose, focus is usually given first on low-order time-space Finite Volume schemes (see [21, 33]).

In this framework, a simple way to compute approximate solutions of system (5) consists in using the following hybrid implicit/explicit time scheme:

$$vol(\Omega_i)\left(W_i^{n+1} - W_i^n - \Delta t^n (S(W))_i^{n+1}\right) = -\int_{\Omega_i}\int_{t^n}^{t^{n+1}} (\nabla \cdot (F(W)) + C(W)\nabla \alpha_l)^n dx dt \tag{60}$$

setting: $\Delta t^n = t^{n+1} - t^n$, noting $vol(\Omega_i)$ the volume of cell Ω_i, and using an explicit approximate Riemann solver associated with the hyperbolic system (evolution step):

$$\partial_t (W) + \nabla \cdot (F(W)) + C(W)\nabla \alpha_l = 0 \tag{61}$$

in order to get $W_i^{\#}$ solution of:

$$vol(\Omega_i)\left(W_i^{\#} - W_i^n\right) + \Delta t^n \int_{\Omega_i} (\nabla \cdot (F(W)) + C(W)\nabla \alpha_l)^n dx = 0 \tag{62}$$

in such a way that the entropy inequality holds true. Afterwards, the solution W_i^{n+1} of the relaxation step:

$$vol(\Omega_i)\left(W_i^{n+1} - W_i^{\#} - \Delta t^n (S(W))_i^{n+1}\right) = 0 \tag{63}$$

must be found within each cell.

This strategy has been used by many authors, in order to compute two-phase or multiphase flows (see among others [6, 18, 26, 55]). Actually, it is rather well-suited for transient flows including shock waves, owing to the fact that:

- the implicit relaxation step enables to get rid of too heavy constraints linked with upper bounds on the time step ;
- the explicit scheme involved in the evolution step is in some sense optimal in terms of accuracy, when focusing on fast pressure waves impinging solid structures, and meanwhile it automatically provides the dynamical time stepping.

Obviously, as it occurs in the single phase framework for weakly compressible flows, other numerical strategies should be preferred when aiming at computing low velocity flows, as proposed for instance quite recently in [56].

Before going further on, we would like to recall some suitable algorithms that provide meaningful approximations in the evolution step (61). Among others, note first that the simple Rusanov solver [57] may be applied for that purpose. Moreover, four distinct schemes providing accurate approximations of the homogeneous part of the Baer-Nunziato model are:

- an approximate Godunov scheme, which has first been proposed in [61] ;
- a relaxation scheme that was then introduced in [15, 58] and extended in [59] for three-phase flow ;
- an HLLC approximate Riemann solver, which was proposed in [64] ;
- another relaxation scheme that was described in [2].

The reader is referred to the paper [14] which provides a detailed comparison of L^1 norm of errors for the latter schemes, while focusing on test cases involving difficult Riemann problems. It also seems worth mentioning the recent Discontinuous Galerkin scheme described in [17]. Eventually, we point out the recent work [63] dedicated to the analysis of the Riemann problem associated with the Baer-Nunziato model.

For all the simulations run in this paper, a robust Rusanov scheme [57] adapted for the handling of non-conservative products is used.

We will now focus on two different strategies in order to get approximations of the set of coupled ODE:

$$\partial_t \left(W \right) = S(W) \tag{64}$$

In the sequel, we will consider:

$$\left\{ \begin{array}{l} \mathscr{V}_I(W) = U_l \\ \Pi_I(W) = P_{g,v} \end{array} \right. \tag{65}$$

2.1 Discrete source terms for gas-liquid flow models

The strategy consists in simulating the drag effects and thermodynamic effects separately. This approach can be justified by the block triangular structure of matrix $\mathscr{R}^{lg}$, see (38). Hence, the simulation of the source terms contains two steps:

$$\text{I:} \quad W^{\#} \xrightarrow{\textit{Velocity relaxation}} W^{n+1-}$$

$$\text{II:} \quad W^{n+1-} \xrightarrow{\textit{Thermodynamic relaxation process}} W^{n+1}$$

The same time step Δt^n is used within each step. The velocity relaxation process is taken from [26] and recalled in **Appendix 2**.

For sake of readability, in sections 2.1 and 2.2, the state W^{n+1-} will be referred as W^n and Δt^n will be mentioned as Δt.

2.1.1 Two approaches for the computation of the thermodynamic source terms

First, we recall that for a quantity Ψ, $\Delta\Psi$ is set as:

$$\Delta\Psi = \Psi_l - \Psi_g \tag{66}$$

Two algorithms are detailed in order to simulate the thermodynamic part of the model (5) in the case of a mix of liquid and gas (i.e. without mass transfer).

A- Fractional step algorithm

A first possible approach in order to account for source terms (34) is to use a fractional step scheme, which decouple (35). System (35), without the velocity relaxation ($d(W) = 0$), is simulated in two implicit steps:

$$\text{I:} \quad W^n \xrightarrow{Pressure\ relaxation} W^{n*}$$
$$\text{II:} \quad W^{n*} \xrightarrow{Heat\ transfer} W^{n+1}$$

The time step Δt, given by the evolution step, is used for computing step I and step II. This idea of decoupling system (34) is quite standard and is already used in the literature (see [56], [25] for example).

I- The pressure relaxation algorithm:

This step is similar but different to the one used in [25]. It simulates the solution of the following system:

$$\begin{cases} \partial_t(\alpha_l) = K(W)\Delta P; \\ \partial_t(m_k) = 0\ ; \quad (k \in \{l,g\}) \\ \partial_t(m_k U_k) = 0\ ; \quad (k \in \{l,g\}) \\ \partial_t(m_l\epsilon_l + m_g\epsilon_g) = 0 \\ m_l\partial_t(\epsilon_l) + P_g\partial_t(\alpha_l) = 0. \end{cases} \tag{67}$$

The equation (67.4) allows writing:

$$\xi_n = m_l^n\epsilon_l^n + m_g^n\epsilon_g^n = m_l^{n*}\epsilon_l^{n*} + m_g^{n*}\epsilon_g^{n*} > 0 \tag{68}$$

Solution of (67) also complies with:

$$\partial_t(S_g) = 0 \tag{69}$$

Thus:

$$S_g^{n*} = S_g^n \tag{70}$$

Using the definition of the sound speed, one can derive from (67):

$$\partial_t(\Delta P) = -a_{PP}\Delta P \tag{71}$$

setting:

$$a_{PP} = K(W)\left(\frac{\rho_l c_l^2}{\alpha_l} + \frac{\rho_g c_g^2}{\alpha_g} - \frac{1}{m_l\partial_{P_l}(\epsilon_l)|_{\rho_l}}\Delta P\right) \tag{72}$$

It can be noted that the coefficient a_{PP} is the one arising in $\mathscr{R}^{lg}$, see (38).

The pressure relaxation algorithm consists in three steps [3].

[3] Given a thermodynamic function Ψ, with some abuse of notation, we still note in the sequel every change of variable of the function $\Psi(P,T) = \hat{\Psi}(\rho,S) = \tilde{\Psi}(P,\rho) = \mathring{\Psi}(P,S) = \ddot{\Psi}(\rho,T)$ as $\Psi(P,T) = \Psi(\rho,S) = \Psi(P,\rho) = \Psi(P,S) = \Psi(\rho,T)$.

Pressure relaxation algorithm:

Step 1: Compute an approximate solution of (71) with an implicit Euler time discretization by considering the frozen coefficient a_{PP} at time t^n:

$$\Delta P^{n*} = \frac{1}{1 + a_{PP}^n \Delta t} \Delta P^n \tag{73}$$

Step 2: Using the constraint (70) on the entropy $S_g^{n*} = S_g^n$ and the conservation law of the sum of the internal energies (67.4), define:

$$\begin{cases} P_g^{n*} := P_l^{n*} - \Delta P^{n*} \\ \rho_g^{n*} := \rho_g(P_g^{n*}, S_g^{n*}) \\ \epsilon_l^{n*} := \dfrac{\xi_n - m_g^n \epsilon_g(P_g^{n*}, S_g^{n*})}{m_l^n} \end{cases} \tag{74}$$

Then compute P_l^{n*} by inverting the immiscible constraint:

$$\frac{m_l^n}{\rho_l(P_l^{n*}, \epsilon_l^{n*})} + \frac{m_g^n}{\rho_g^{n*}} - 1 = 0 \Leftrightarrow G(P_l^{n*}) = 0 \tag{75}$$

Step 3: Update the statistical fractions α_l^{n*} and α_g^{n*}:

$$\begin{cases} \alpha_l^{n*} = \dfrac{m_l^n}{\rho_l(P_l^{n*}, \epsilon_l^{n*})} \\ \alpha_g^{n*} = 1 - \alpha_l^{n*} \end{cases} \tag{76}$$

and the total energies:

$$\begin{cases} \alpha_l^{n*} E_l^{n*} = m_l^n \epsilon_l^{n*} + \dfrac{1}{2} m_l^n (U_l^n)^2 \\ \alpha_g^{n*} E_g^{n*} = \alpha_l^n E_l^n + \alpha_g^n E_g^n - \alpha_l^{n*} E_l^{n*} \end{cases} \tag{77}$$

□

Thus, we have:

Property 4: (Pressure relaxation algorithm)

- *The pressure relaxation process is effective during step 1 if the pressure gap satisfies condition* (44).
- *For any mixture of two generalized stiffened gas EOS, the solution* P_l^{n*} *of step 2, in the admissible range, exists and is unique. Moreover,* $\alpha_l^{n*} \in [0, 1]$.

□

Proof. :

- If the pressure gap satisfies (44), then the coefficient a_{PP} is positive and the discrete equation (73) is a contraction whatever the time step is.
- Let us consider a mixture of two generalized stiffened gases:

$$\begin{cases} (\gamma_k - 1)\rho_k(\epsilon_k - \epsilon_{k_0}) = P_k + \gamma_k \hat{\Pi}_k \\ S_k - s_{k_0} = C_{v_k} log\left((\epsilon_k - \epsilon_{k_0} - \dfrac{\hat{\Pi}_k}{\rho_k}) \rho_k^{1-\gamma_k} \right) \end{cases} \tag{78}$$

with $\hat{\Pi}_k$ a positive constant and ϵ_{k_0} and s_{k_0} constants.

Let us recall the constraint for the pressure in the case of a generalized stiffened gas:

$$P_k + \hat{\Pi}_k > 0 \tag{79}$$

Thanks to (70), one can obtain:

$$\alpha_g^{n*} = m_g^n \frac{(\gamma_k - 1)^{\frac{1}{\gamma_k}} \exp(\frac{S_g^n - s_{g_0}}{\gamma_g C_{v_g}})}{\left(P_l^{n*} - \Delta P^{n*} + \hat{\Pi}_g\right)^{\frac{1}{\gamma_g}}} \tag{80}$$

By enforcing (67.4) one can deduce:

$$\epsilon_l^{n*} = \frac{1}{m_l^n}\left(\xi_n - \alpha_g^{n*}\ \frac{P_l^{n*} - \Delta P^{n*} + \gamma_g \hat{\Pi}_g}{\gamma_g - 1} - m_g^n \epsilon_{g_0}\right) \tag{81}$$

The immiscible constraint (1) can then be rewritten as follows:

$$\frac{(\gamma_l - 1)\left((m_l\epsilon_l)^{n*} - m_l^n \epsilon_{l_0}\right)}{P_l^{n*} + \gamma_l \hat{\Pi}_l} + m_g^n (\gamma_g - 1)^{1/\gamma_g} \frac{\exp(\frac{S_g^n - s_{g_0}}{\gamma_g C_{v_g}})}{\left(P_l^{n*} - \Delta P^{n*} + \hat{\Pi}_g\right)^{\frac{1}{\gamma_g}}} - 1 = 0 \tag{82}$$

Which can be seen as:

$$H(P_l) = 0 \tag{83}$$

Standard calculations show that the function H is decreasing and, using (79), that the bounds are:

$$\begin{cases} \lim\limits_{P_l \to +\infty} H(P_l) = -1 \\ \lim\limits_{P_l \to max(-\hat{\Pi}_l, \Delta P - \hat{\Pi}_g)} H(P_l) = +\infty \end{cases} \tag{84}$$

which enables to conclude for P_l^{n*}, such that $P_l^{n*} + \Pi_l > 0$ and $P_g^{n*} + \Pi_g > 0$.

Thus, $\alpha_l^{n*} \in [0, 1]$, owing to (80) and (82).

□

II- The temperature relaxation algorithm:

It simulates the solutions of the following system:

$$\begin{cases} \partial_t(\alpha_l) = 0 \\ \partial_t(m_k) = 0 \quad (k \in \{l, g\}) \\ \partial_t(m_k U_k) = 0 \quad (k \in \{l, g\}) \\ \partial_t(m_l\epsilon_l + m_g\epsilon_g) = 0 \\ m_l \partial_t(\epsilon_l) + P_g \partial_t(\alpha_l) = -q(W)\Delta T. \end{cases} \tag{85}$$

The evolution of the temperature gap ΔT can be deduced from (85), it reads:

$$\partial_t(\Delta T) = -a_{TT}\Delta T \tag{86}$$

setting:

$$a_{TT} = q(W)\left(\frac{1}{m_l \partial_{T_l}(\epsilon_l)|_{\rho_l}} + \frac{1}{m_g \partial_{T_g}(\epsilon_g)|_{\rho_g}}\right) \tag{87}$$

With a_{TT} arising in the matrix $\mathscr{R}^{lg}$, see (38).

The temperature relaxation algorithm consists in three steps.

Temperature relaxation algorithm:

Step 1: Compute an approximate solution of the equation (86) with an implicit Euler time discretization by considering the coefficient a_{TT} frozen at the time t^{n*}:

$$\Delta T^{n+1} = \frac{1}{1 + a_{TT}^{n*}\Delta t}\Delta T^{n*} \tag{88}$$

Step 2: Since α_l is constant throughout this step, and considering the conservation law of the sum of the internal energies (85.4), T_l^{n+1} is solution of:

$$m_l^n \epsilon_l(\rho_l^{n*}, T_l^{n+1}) + m_g^n \epsilon_g(\rho_g^{n*}, T_l^{n+1} - \Delta T^{n+1}) = \xi_n \tag{89}$$

Step 3: Update the thermodynamic quantities $T_g^{n+1} = T_l^{n+1} - \Delta T^{n+1}$, and the total energies:

$$\begin{cases} (\alpha_l E_l)^{n+1} = m_l^n \epsilon_l(\rho_l^{n*}, T_l^{n+1}) + \dfrac{1}{2} m_l^n (U_l^n)^2 \\ (\alpha_g E_g)^{n+1} = \alpha_l^{n*} E_l^{n*} + \alpha_g^{n*} E_g^{n*} - \alpha_l^{n+1} E_l^{n+1} \end{cases} \tag{90}$$

▫

We get:

Property 5: (Temperature relaxation algorithm)

- *Step 1 guaranties the relaxation process for the temperature throughout this algorithm, whatever the time step is.*
- *Considering a mixture of two generalized stiffened gas EOS, the solution T_l^{n+1} of step 2 in the admissible range exists and is unique.*

▫

Proof. :

- As the coefficient a_{TT} is positive, the discretized equation of evolution of ΔT (88) is a contraction.
- For a mixture of two generalized stiffened gases, the temperature at time t^{n+1} is:

$$T_l^{n+1} = \frac{1}{m_l^n C_{v_l} + m_g^n C_{v_g}} \left(\xi_n + m_g^n C_{v_g} \Delta T^{n+1} - (m_l^n \epsilon_{l_0} + m_g^n \epsilon_{g_0} + \hat{\Pi}_l \alpha_l^{n*} + \hat{\Pi}_g (1 - \alpha_l^{n*})) \right) \tag{91}$$

□

B- Coupled algorithm

The basic idea of this new algorithm consists in simulating the thermodynamic relaxation effects in one step. The governing set of equations is as follows:

$$\begin{cases} \partial_t (m_k) = 0 \quad (k \in \{l, g\}) \\ \partial_t (m_k U_k) = 0 \quad (k \in \{l, g\}) \\ \partial_t (m_l \epsilon_l + m_g \epsilon_g) = 0 \\ \partial_t (\alpha_l) = K(W) \Delta P \\ m_l \partial_t (\epsilon_l) + P_g \partial_t (\alpha_l) = -q(W) \Delta T \end{cases} \tag{92}$$

Using (92) one can obtain:

$$\partial_t \begin{pmatrix} \Delta P \\ \Delta T \end{pmatrix} = -\mathscr{R}_{PT} \begin{pmatrix} \Delta P \\ \Delta T \end{pmatrix} \tag{93}$$

with:

$$\mathscr{R}_{PT} = \begin{pmatrix} a_{PP} & a_{PT} \\ a_{TP} & a_{TT} \end{pmatrix} \tag{94}$$

Matrix $\mathscr{R}_{PT}$ is a sub-matrix of matrix $\mathscr{R}^{lg}$ (38):

$$\left\{ \begin{array}{l} a_{PP} = K(W) \left(A_l + A_g - \dfrac{1}{m_l \partial_{P_l}(\epsilon_l)\,|_{\rho_l}} \Delta P \right) \\ a_{PT} = q(W) \left(\dfrac{1}{m_l \left.\frac{\partial \epsilon_l}{\partial P_l}\right|_{\rho_l}} + \dfrac{1}{m_g \left.\frac{\partial \epsilon_g}{\partial P_g}\right|_{\rho_g}} \right) \\ a_{TP} = K(W) \left[\left(\left.\dfrac{\partial \epsilon_l}{\partial T_l}\right|_{\rho_l} \right)^{-1} \left(\dfrac{P_g}{m_l} - \dfrac{\rho_l}{\alpha_l} \left.\dfrac{\partial \epsilon_l}{\partial \rho_l}\right|_{T_l} \right) + \left(\left.\dfrac{\partial \epsilon_g}{\partial T_g}\right|_{\rho_g} \right)^{-1} \left(\dfrac{P_g}{m_g} - \dfrac{\rho_g}{\alpha_g} \left.\dfrac{\partial \epsilon_g}{\partial \rho_g}\right|_{T_g} \right) \right] \\ a_{TT} = q(W) \left(\dfrac{1}{m_l \partial_{T_l}(\epsilon_l)\,|_{\rho_l}} + \dfrac{1}{m_g \partial_{T_g}(\epsilon_g)\,|_{\rho_g}} \right) \end{array} \right. \tag{95}$$

The coupled algorithm reads as follows:

Coupled (P-T) relaxation algorithm:

Step 1: Compute an approximate solution of system (93), with the evolution matrix $\mathscr{R}_{PT}$ frozen at time t^n, using an implicit Euler scheme:

$$\begin{pmatrix} \Delta P \\ \Delta T \end{pmatrix}^{n+1} = (\mathscr{I}_2 + \Delta t\ \mathscr{R}^n_{PT})^{-1} \begin{pmatrix} \Delta P \\ \Delta T \end{pmatrix}^n \tag{96}$$

where $\mathscr{I}_2$ is the identity matrix in $\mathscr{M}_2(\mathbb{R})$.

Step 2: Set:

$$\left\{ \begin{array}{l} \xi_n = m_l \epsilon_l(P_l^n, T_l^n) + m_g \epsilon_g(P_g^n, T_g^n) \\ T_g^{n+1} = T_l^{n+1} - \Delta T^{n+1} \\ P_g^{n+1} = P_l^{n+1} - \Delta P^{n+1} \end{array} \right. \tag{97}$$

Compute P_l^{n+1} and T_l^{n+1}, solutions of the following system:

$$\left\{ \begin{array}{l} m_l^n \epsilon_l(P_l^{n+1}, T_l^{n+1}) + m_g^n \epsilon_g(P_g^{n+1}, T_g^{n+1}) = \xi_n \\ \dfrac{m_l^n}{\rho_l(P_l^{n+1}, T_l^{n+1})} + \dfrac{m_g^n}{\rho_g(P_g^{n+1}, T_g^{n+1})} = 1 \end{array} \right. \tag{98}$$

Step 3: Update α_l^{n+1}:

$$\alpha_l^{n+1} = \frac{m_l^n}{\rho_l(P_l^{n+1}, T_l^{n+1})} \tag{99}$$

and the total energies:

$$\left\{ \begin{array}{l} (\alpha_l E_l)^{n+1} = m_l^n \epsilon_l(P_l^{n+1}, T_l^{n+1}) + \dfrac{1}{2} m_l^n (U_l^n)^2 \\ (\alpha_g E_g)^{n+1} = \alpha_l^n E_l^n + \alpha_g^n E_g^n - (\alpha_l E_l)^{n+1} \end{array} \right. \tag{100}$$

□

Before going further on, we introduce the following lemma:

Lemma 1:
For a system of the form:

$$\partial_t Y(W) = -A(W)Y(W) \tag{101}$$

with $Y \in \mathbb{R}^j$ and $A \in \mathscr{M}_j(\mathbb{R})$, $j \in \mathbb{N}$, discretized by using an implicit Euler scheme as:

$$(\mathscr{I}_j + \Delta t A^n)Y^{n+1} = Y^n \tag{102}$$

with $\mathscr{I}_j$ the identity of $\mathscr{M}_j(\mathbb{R})$. If the real part of every eigenvalue of A^n is positive, then system (102) ensures that:

$$\|Y^{n+1}\|_2 \leqslant \|Y^n\|_2 \tag{103}$$

and that system (102) is invertible, whatever the time step is.

Proof. :

As $A^n \in \mathscr{M}_j(\mathbb{R})$, its eigenvalues $\lambda_1, \ldots, \lambda_j$ are in $\mathbb{C}$:

$$\forall k \in [\![1, j]\!] \ , \ \lambda_k = a_k + ib_k \tag{104}$$

Then, the eigenvalues $\lambda_1^r, \ldots, \lambda_j^r$ of the matrix $(I_j + \Delta t A^n)^{-1}$ are:

$$\forall k \in [\![1, j]\!] \ , \ \lambda_k^r = \frac{1}{1 + a_k \Delta t + ib_k \Delta t} \tag{105}$$

Assuming that the real parts of the eigenvalues of A^n are positive:

$$\forall k \in [\![1, j]\!] \ , \ a_k > 0 \tag{106}$$

then,

$$\forall \Delta t > 0 \ , \ \forall k \in [\![1, j]\!] \ , \ |1 + a_k \Delta t + ib_k \Delta t| > 1 \ . \tag{107}$$

Whatever the time step is, this ensures that system (102) is invertible and that:

$$\|Y^{n+1}\|_2 \leqslant \|Y^n\|_2 \tag{108}$$

□

Then, one can obtain:

Property 6: (Coupled P-T relaxation algorithm)

- *If the pressure gap satisfies condition (44), then equation (96) ensures the relaxation process of the pressure and the temperature over time whatever the time step is, if (45) holds.*
- *Given a mixture of two perfect gas EOS, the solution of (98) in the admissible range, exists and is unique. Moreover, the discrete statistical fraction α_l^{n+1} belongs to $[0, 1]$.*

▫

Proof. :

- If conditions (44) and (45) are verified, then the real parts of the eigenvalues of $\mathscr{R}_{PT}$ are positive. Thus, **Lemma 1** applies and equation (96) ensures the relaxation process over time, whatever the time step is.

- Let us consider a mixture of two perfect gases:

$$\begin{cases} (\gamma_k - 1)\rho_k \epsilon_k = P_k \\ \epsilon_k = C_{v_k} T_k \end{cases} \tag{109}$$

Then it can be deduced from the conservation law of the sum of the internal energies (92.3) that:

$$T_l^{n+1} = \frac{\xi_n + m_g^n \; C_{v_g} \Delta T^{n+1}}{m_l^n \; C_{v_l} + m_g^n \; C_{v_g}} \tag{110}$$

Inserting (109) and (110) in (98.2), one can obtain:

$$\Theta(P_l^{n+1}) = \frac{m_l^n (\gamma_l - 1) C_{v_l} T_l^{n+1}}{P_l^{n+1}} + \frac{m_g^n (\gamma_g - 1) C_{v_g} (T_l^{n+1} - \Delta T^{n+1})}{P_l^{n+1} - \Delta P^{n+1}} - 1 = 0 \tag{111}$$

Standard calculations show that the function $\Theta(P_l)$ is decreasing and that its bounds are:

$$\begin{cases} \lim\limits_{P_l \to +\infty} \Theta(P_l) = -1 \\ \lim\limits_{P_l \to max(0, \Delta P)} \Theta(P_l) = +\infty \end{cases} \tag{112}$$

which enables to conclude for P_l^{n*}, such that $P_l^{n*} + \Pi_l > 0$ and $P_g^{n*} + \Pi_g > 0$. Moreover, as $k \in \{l, g\}$, $T_k = \dfrac{P_k + \Pi_k}{\rho_k C_{v_k} (\gamma_k - 1)}$, temperatures T_l and T_g are in the admissible range.

Thus, $\alpha_l^{n*} \in [0, 1]$, owing to (111).

□

Remark 2: For a mixture of Stiffened Gas EOS, system (98) is fully coupled. Equation (98.1) writes:

$$\begin{cases} T_l^{n+1} \left(m_l^n C_{v_l} \left[1 + \dfrac{(\gamma_l - 1)\hat{\Pi}_l}{P_l^{n+1} + \hat{\Pi}_l} \right] + m_g^n C_{v_g} \left[1 + \dfrac{(\gamma_g - 1)\hat{\Pi}_g}{P_l^{n+1} - \Delta P^{n+1} + \hat{\Pi}_g} \right] \right) = \xi_n + \hat{E}_{n+1} \\ \hat{E}_{n+1} = -m_l^n \epsilon_{l_0} - m_g^n \epsilon_{g_0} + m_g^n C_{v_g} \Delta T^{n+1} \left[1 + \dfrac{(\gamma_g - 1)\hat{\Pi}_g}{P_l^{n+1} - \Delta P^{n+1} + \hat{\Pi}_g} \right] \end{cases} \tag{113}$$

Moreover, equation (98.2) reads:

$$m_l^n \frac{(\gamma_l - 1) C_{v_l} T_l^{n+1}}{P_l^{n+1} + \hat{\Pi}_l} + m_g^n \frac{(\gamma_g - 1) C_{v_g} (T_l^{n+1} - \Delta T^{n+1})}{P_l^{n+1} - \Delta P^{n+1} + \hat{\Pi}_g} = 1 \tag{114}$$

2.1.2 Verification and comparison between the two approaches in a homogeneous case

The basic idea for the two approaches detailed before is to deduce from system (34) an equation of evolution of the gap of the thermodynamics quantities. The main advantage of this idea is that it can ensure the relaxation process between the phases over time, giving conditions that can be easily verified inside a code. The main difference is whether system (34) is simulated in one step or "decoupled". In this section, the two approaches are numerically compared. To do so, the flow is supposed to be homogeneous:

$$\forall \Psi(W), \; \partial_x \Psi(W) = 0 \tag{115}$$

and velocities within each phase are assumed to be null. This simulation can be viewed as the return to thermodynamics equilibrium of a two-phase flow inside a box. The different simulations are performed with time steps ranging between 10^{-10} s and 10^{-2} s. All relaxation time scales are supposed to be constant. Their values, the initial conditions and the coefficients of the EOS for the different cases are given in **Appendix 1**. Moreover, in order to ensure an effective relaxation time of each separated effect close to the relaxation time scale given by the user, the value of $\mathscr{P}_0$ has to be set at $t = 0$ to:

$$\mathscr{P}_0 = \| \alpha_v^0 \rho_l^0 (c_l^0)^2 + \alpha_l^0 \rho_v^0 (c_v^0)^2 - \alpha_v^0 \frac{\Delta P^0}{\rho_l^0 \left(\partial_{P_l} (\epsilon_l) |_{\rho_l} \right)^0} \| \tag{116}$$

The fractional step algorithm obviously does not capture the correct behaviour of the pressure P_l at the origin for coarse time steps in some cases (see **Figure** 1). Actually, it can lead to a huge overestimation of the pressure, whereas the coupled algorithm better follows the monotony of the exact solution (see **Figure** 2). For example, in **Figure** 1, the pressure P_l for large time steps can be ten times bigger than the one obtained with the coupled approach. The relaxation process overtime is effective in case 1 as it can be seen in **Figures** 3 and 4. Here, owing to (50), and since $\hat{\Pi}_l > \hat{\Pi}_g$, condition (44) is automatically satisfied. Nonetheless, condition (45) must be checked inside the code -see **Section** 1.3-. **Figures** 5 and 6 show that the two numerical methods give similar results on the temperature profiles in this case. The main difference between the two numerical approaches here lays in the liquid pressure profiles.

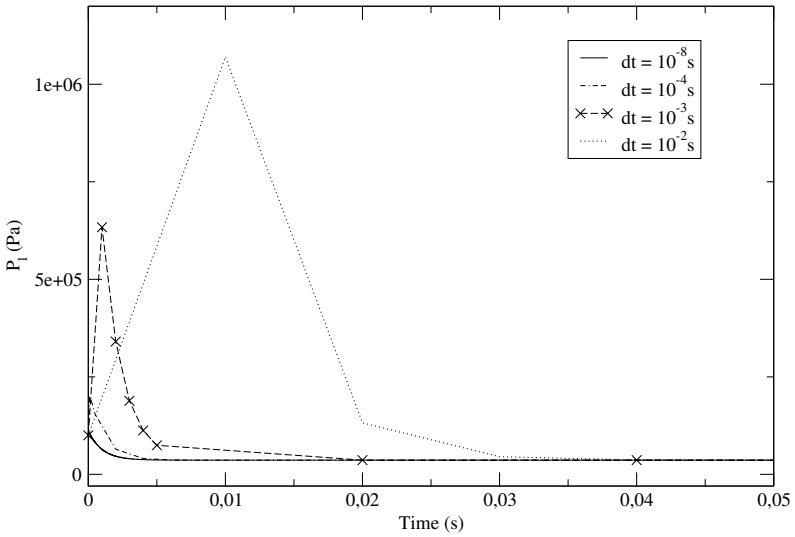

Figure 1: Homogeneous case: evolution of the pressure P_l in case 1 ($\tau_P = 10^{-5}$s and $\tau_T = 10^{-3}$s), computed with the fractional step algorithm. The initial conditions are given in **Appendix 1**.

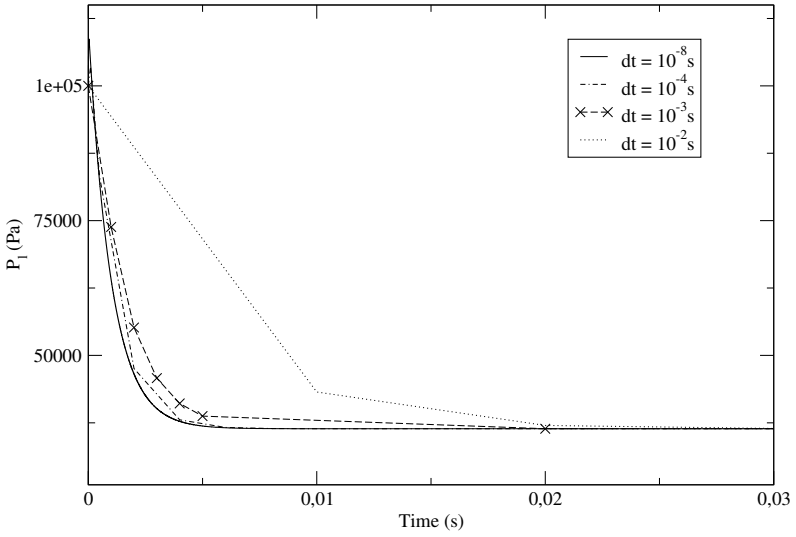

Figure 2: Homogeneous case: evolution of the pressure P_l in case 1 ($\tau_P = 10^{-5}$s and $\tau_T = 10^{-3}$s), computed with the coupled algorithm. The initial conditions are given in **Appendix 1**.

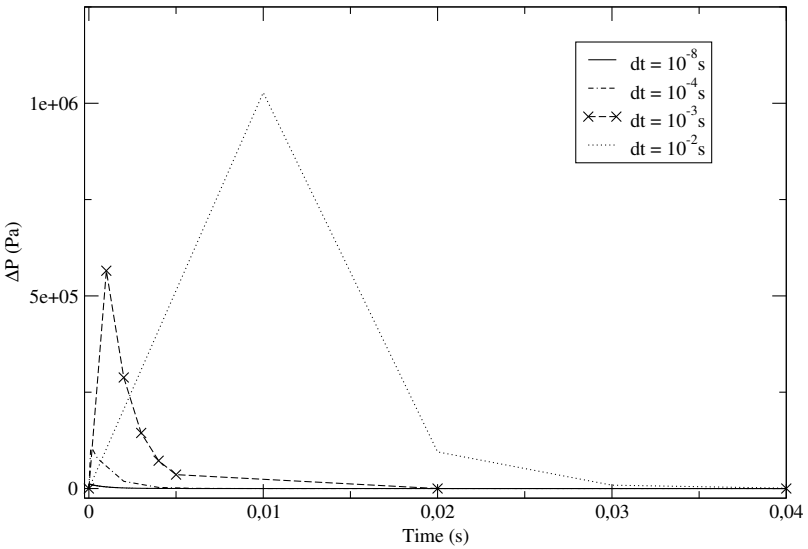

Figure 3: Homogeneous case: evolution of $\Delta P = P_l - P_g$ in case 1 ($\tau_P = 10^{-5}$s and $\tau_T = 10^{-3}$s), computed with the fractional step algorithm. The initial conditions are given in **Appendix 1**.

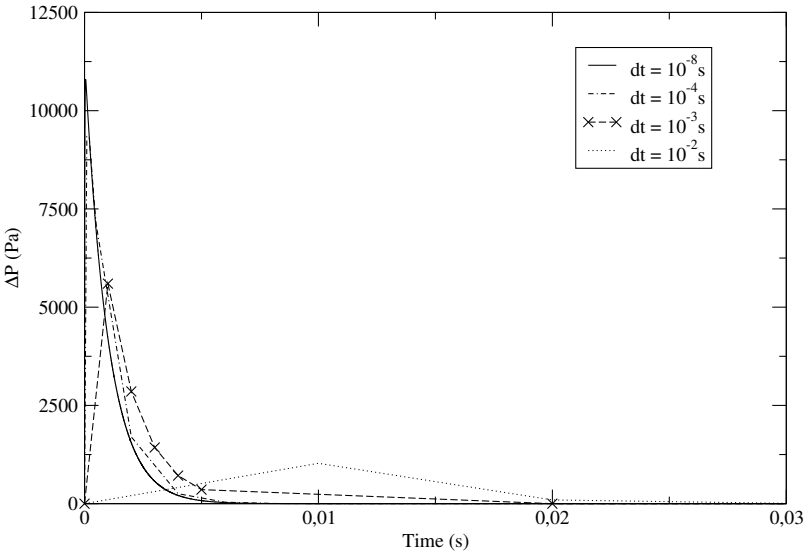

Figure 4: Homogeneous case: evolution of $\Delta P = P_l - P_g$ in case 1 ($\tau_P = 10^{-5}$s and $\tau_T = 10^{-3}$s), computed with the coupled algorithm. The initial conditions are given in **Appendix 1**.

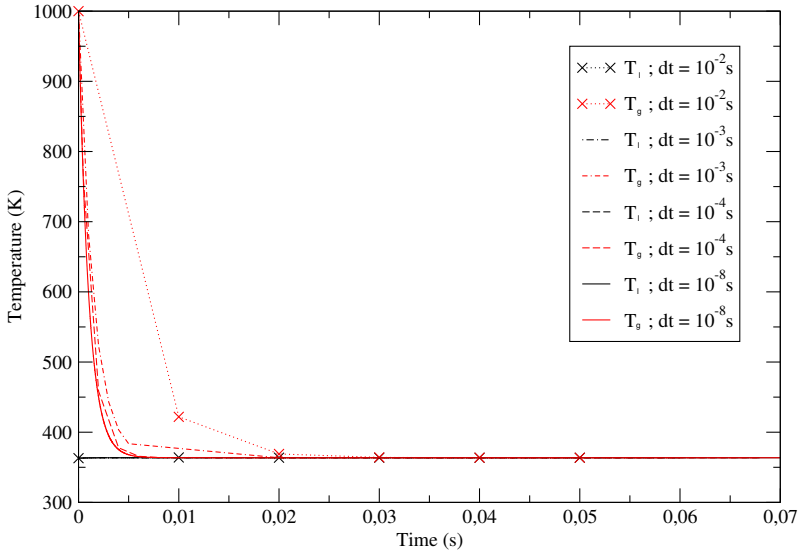

Figure 5: Homogeneous case: evolution of T_l and T_g in case 1 ($\tau_P = 10^{-5}$s and $\tau_T = 10^{-3}$s), computed with the fractional step algorithm. The initial conditions are given in **Appendix 1**.

In order to evaluate the performance of these two numerical schemes, a convergence study has been conducted. Let us introduce the error $E_\Psi(t, \Delta t)$ of a thermodynamic quantity Ψ for a time step Δt at time t. Given the numerical approximate solution Ψ_{ap} of Ψ_{ex}, the error $E_\Psi(t, \Delta t)$ is calculated as follows:

$$E_\Psi(t_t, \Delta t) = \frac{|\Psi_{ex}(t_t) - \Psi_{ap}(N\Delta t)|}{|\Psi_{ex}(t = 0)|} \tag{117}$$

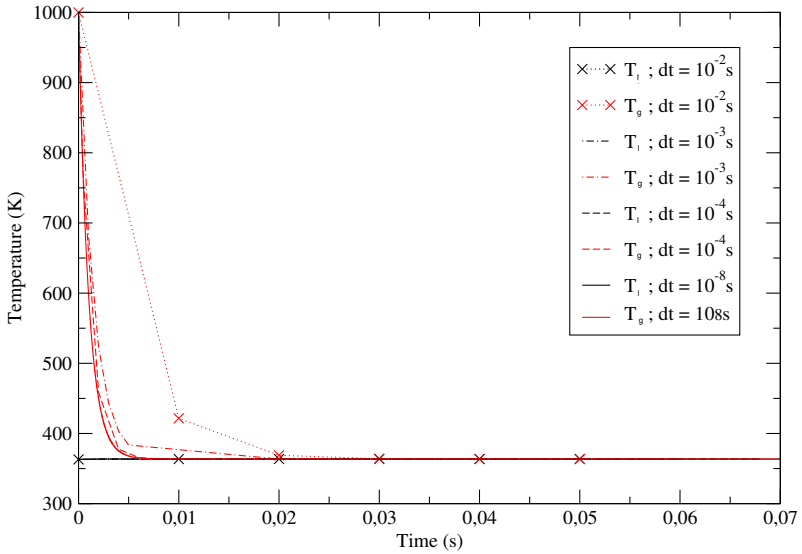

Figure 6: Homogeneous case: evolution of T_l and T_g in case 1 ($\tau_P = 10^{-5}$s and $\tau_T = 10^{-3}$s), computed with the coupled algorithm. The initial conditions are given in **Appendix 1**.

with:

$$t_t = N\Delta t. \tag{118}$$

In our cases we set $t_t = 2.0\ 10^{-3}$s.

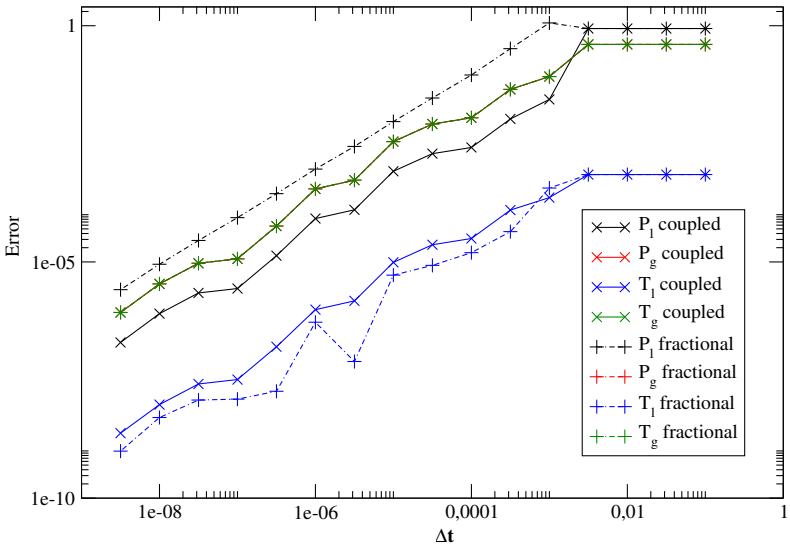

Figure 7: Homogeneous case: Convergence curve for case 1. The initial conditions are given in **Appendix 1**.

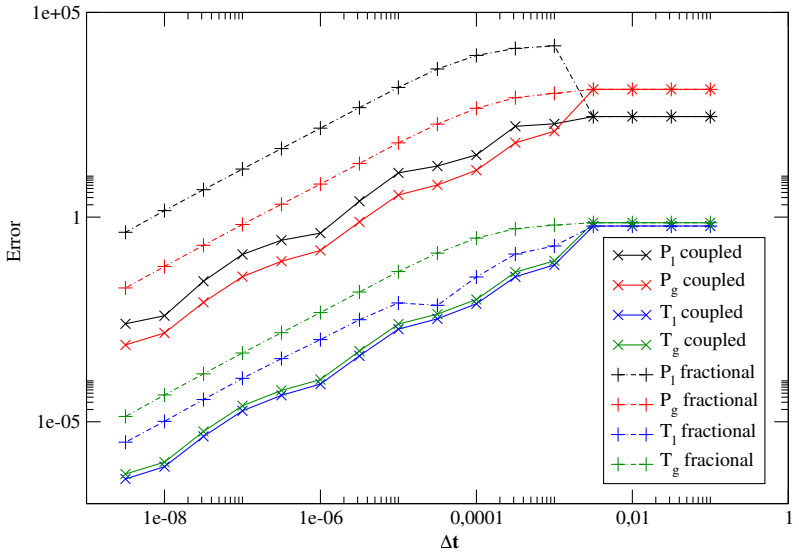

Figure 8: Homogeneous case: Convergence curve for case 5. The initial conditions are given in **Appendix 1**.

The convergence curves (see **Figures** 7 and 8) show a speed of convergence close to 1 for the two approaches, as expected theoretically. It is worth noting that the value of the error can be quite large for the fractional step algorithm, as it can be two hundred times bigger than the error of the coupled algorithm for the pressure P_l, see **Figure** 8. The plateau of convergence for large time steps corresponds to simulations where $\mathbf{\Delta t > t_t}$.

Moreover, for a given value of Δt, the ratio of computational costs is between 2 and 8 in favour of the coupled algorithm, depending on the mesh size, see **Table** 1.

dt	Coupled algorithm	Fractional algorithm
$10^{-2}s$	2.92 10^{-6}	7.51 10^{-6}
$10^{-4}s$	6.26 10^{-5}	1.26 10^{-4}
$10^{-6}s$	1.38 10^{-3}	1.1 10^{-2}
$10^{-8}s$	1.21 10^{-1}	1

Table 1: CPU normalised by the CPU of the fractional step algorithm using $\Delta t = 10^{-8}s$ for case 1

Remark 3: It is also worth noting that the accuracy of the fractional step algorithm decreases when the ratio $\frac{\tau_P}{\tau_T}$ tends to zero (see **Appendix** 7).

2.1.3 Application: shock wave through a two-phase gas-liquid medium [12]

A- Experimental set up and numerical settings:

This part aims at validating the coupled scheme by comparing its results with the experiment [12] (see [10] for further details). The experimental set-up is made up of a one-dimensional shock tube composed of air and a layer of liquid droplets. It contains, at $t = 0$ (see **Figure** 9 for a sketch of this set up), a high pressure

chamber (HP), followed by a zone at atmospheric pressure. Inside the low pressure chamber, a cloud of droplets (CD) with a unique diameter ($D_d = 500\mu m$) lies between $x = 3.0m$ and $x = 3.40m$.

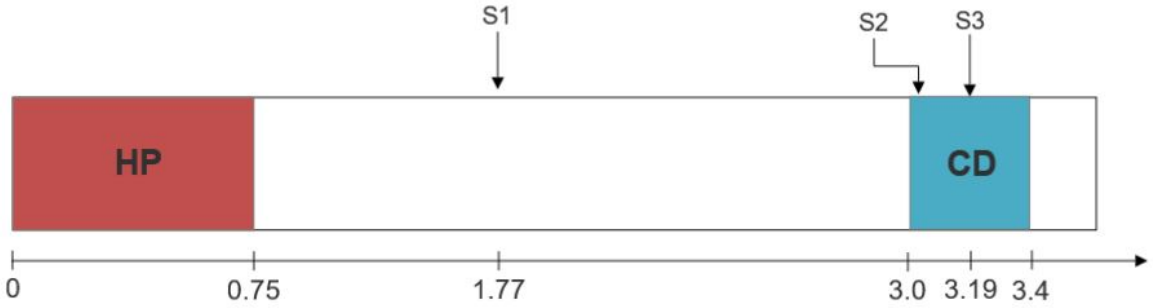

Figure 9: Sketch of the data settings in meters

The initial conditions are set as follows [12]:

Abscissa interval (m)	P_l (bar)	P_g (bar)	α_l	α_g	T_l (K)	T_g (K)
$x \in [0.0\ , 0.75]$	7	7	$\epsilon_\alpha = 10^{-10}$	$1 - \epsilon_\alpha$	293	293
$x \in [3.0\ , 3.4]$	1	1	0.0104	0,9896	293	293
$x \in]0.75\ , 3.0[\cup]3.4\ , 3.75])$	1	1	ϵ_α	$1 - \epsilon_\alpha$	293	293

In the experimental set-up, several pressure probes are set throughout the tube [12]. They give the value of the total pressure. The total pressure P_{mix} is defined as:

$$P_{mix} = \sum_k \alpha_k P_k \tag{119}$$

Indeed, setting:

$$Q = \sum_k m_k U_k \tag{120}$$

and using (5), we have:

$$\partial_t (Q) + \nabla \cdot (\sum_k m_k U_k \otimes U_k) + \nabla P_{mix} = 0 \tag{121}$$

Integrating (121) over a closed domain shows that the pressure applied on the walls is precisely P_{mix}, *i.e.* the total pressure measured experimentally.

The value of P_{mix} is compared with the experimental data on three probes:

- S_1 located at $x = 1.77m$. This station is located inside the initial gaseous area.
- S_2 located at $x = 3.08m$. This station is located at the beginning of the initial layer of droplets.
- S_3 located at $x = 3.19m$. This station is located in the middle of the initial cloud of droplets.

In this configuration, the fragmentation of the water droplets plays a substantial role in the dynamic, according to [31]. That is why an interfacial area $\mathscr{A}$ is introduced for the liquid phase:

$$\mathscr{A} = \frac{6\alpha_l}{D_d} \tag{122}$$

The equation of evolution of the interfacial area (see **Appendix 3**) and its numerical treatment are taken from [5]. The velocity relaxation process has to be computed too. To do so, the algorithm detailed in [26] has been used and is recalled in **Appendix 2**. In order to simulate this shock tube, stiffened gas EOS (see (78)) are used in each phase. The values of the thermodynamic coefficients are given in **Appendix 1**.

Moreover, the relaxation time scales τ_U, τ_P and τ_T are chosen as follows.

Velocity relaxation time scale:

$$\frac{1}{\tau_U} = \frac{0.125(m_l + m_g)\|U_l - U_g\|}{\rho_l D_d}; \tag{123}$$

This expression of τ_U is derived from the Stokes formula [46].

Pressure relaxation time scale:

$$\tau_P \mathscr{P}_0 = \frac{4\pi}{3}\mu_g \Leftrightarrow \frac{1}{\tau_P} = \frac{3\mathscr{P}_0}{4\pi\mu_g} \tag{124}$$

where $\mu_g = 1.8\ .10^{-5}\ kgm^{-1}s^{-1}$ is the dynamic viscosity of the air at 1 bar and 293K. It is the limit of the closure law proposed in [28] for small diameter droplets.

Temperature relaxation time scale:

$$\frac{1}{\tau_T} = \frac{6\alpha_l Nu\lambda_g(m_l C_{v_l} + m_g C_{v_g})}{m_l C_{v_l} m_g C_{v_g} D_d^2}; \tag{125}$$

where Nu = 10 is the Nusselt number and $\lambda_g = 0.6\ (Wm^{-1}K^{-1})$ is the thermal conductivity of the gas phase. This form is taken from [54].

The simulations have been performed using one-dimensional meshes including 1 000, 10 000 and 20 000 cells. The CFL number is set to 0.45 and provides the time stepping.

B- Numerical results and comparison with experimental data:

We recall that the Weber number, We, is a dimensionless number that quantifies the atomization of the droplets. Introducing σ_d, a positive reference surface tension, We is defined as:

$$We = \frac{\rho_l \|U_l - U_g\|^2 D_d}{\sigma_d}. \tag{126}$$

More precisely, if the Weber number is smaller than a certain threshold called the critical Weber number We_c, then the atomization does not occur (see **Appendix 3**). Two critical Weber numbers will be tested in the simulations: $We_c = 3$ and $We_c = 12$. These values, respectively suggested for liquid water and liquid aluminium droplets, are taken from [54]. The total pressure P_{mix} obtained through numerical simulations is compared with the experimental data.

First, let us note that on **Figures** 10, 11 and 12, the experimental data have been translated of a fixed value $t_{translate} = 0.0019s$, so that the experimental and simulated incident shock waves are synchronized on station 3. As the experimental and numerical shock waves arrive almost at the same time at the station 1 and 2, it can be concluded that the simulation captures well the celerity of the shock wave. On fine meshes, **Figures** 10 and 11 show a pressure drop right after the incident shock wave of 2.4 bar. The amplitude of the incident shock wave is overestimated by the simulation by 10% at station 3 (**Figure** 10), whereas there is almost no discrepancy between the simulation and the experimental data at stations 1 and 2. The pressure loss right

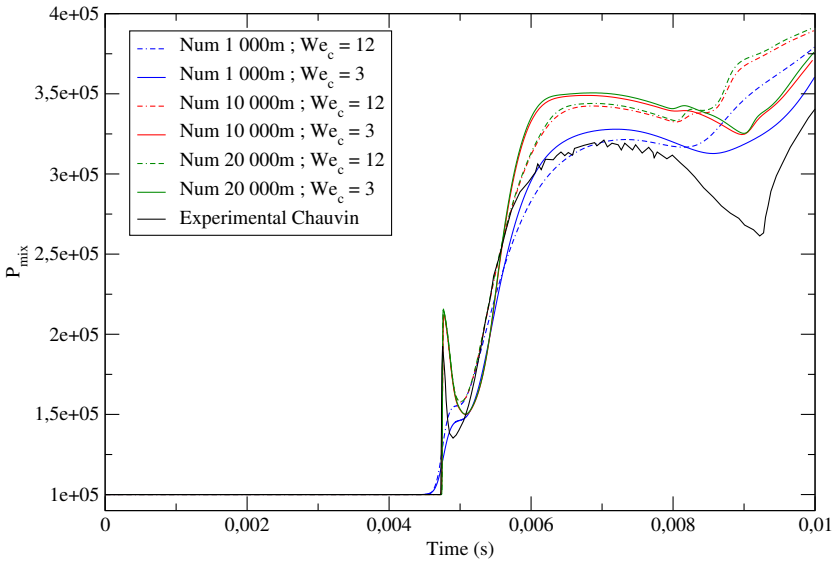

Figure 10: Chauvin experiment: Evolution of the pressure $P_{mix}(Pa) = \alpha_l P_l + \alpha_g P_g$ at station 3, using two different critical Weber numbers: $We_c = 3$ or 12. Meshes contain: 1 000 cells, 10 000 cells or 20 000 cells. CFL = 0.45 .

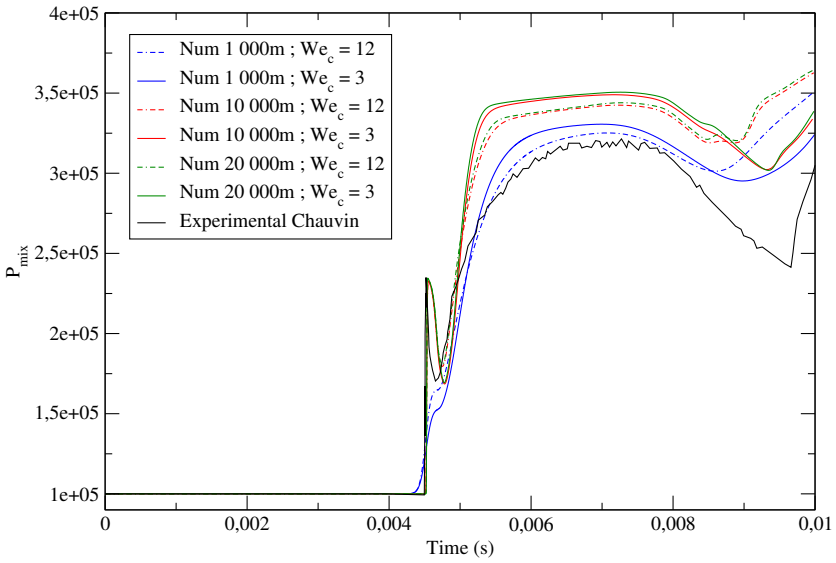

Figure 11: Chauvin experiment: evolution of the pressure $P_{mix}(Pa)$ at station 2 for various meshes and We_c

after the shock wave is expected as it accounts for the atomization of the water droplets, see [31]. A coarse mesh with 1000 cells is not sufficient to properly capture this phenomenon. In **Figure** 10, after the pressure loss, the total pressure increases and then plateaus around $3.5bar$, considering $We_c = 3$ and a 20 000 cells mesh. Focusing on this mesh, the numerical results overestimate the experimental data on P_{mix} by about 7 % on station 3, 10 % on station 2 and 2 % on station 1. Eventually, the total pressure decreases due to the

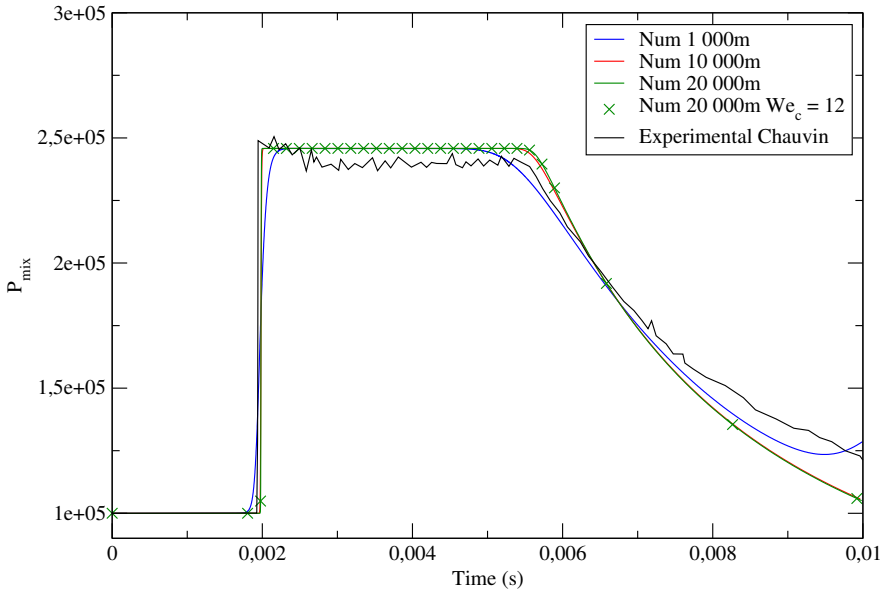

Figure 12: Chauvin experiment: evolution of the pressure $P_{mix}(Pa)$ at station 1 for various meshes

arrival of the reflected rarefaction wave coming from the left wall boundary. It is also worth noting that ΔP remains lower than 2. 10^{-3} % of the initial phasic pressure throughout the simulation. On the other hand, ΔT remains lower than 2 % of the initial phasic temperature gap.

The numerical simulation of Chauvin experiment [12] using the fractional step approach can be found in section 4.3 of [6]. On a fine mesh, discrepancies between the two approaches on the total pressure profile are less than 1 % on the incident shock wave amplitude, and about 5 % on the pressure plateau.

In addition, these numerical simulations also show the influence of the critical Weber number - *i.e.* how the interfacial area is taken into account - on the overall behaviour of the solution after the shock wave, inside the cloud of collapsible droplets. Indeed, as shown in [11], an accurate modelling of the inter-facial area evolution is a key ingredient in order to capture the correct behaviour of the pressure profile after the shock. Herein, computational results are closer to the experimental data when using $We_c = 3$ on a refined mesh, as anticipated.

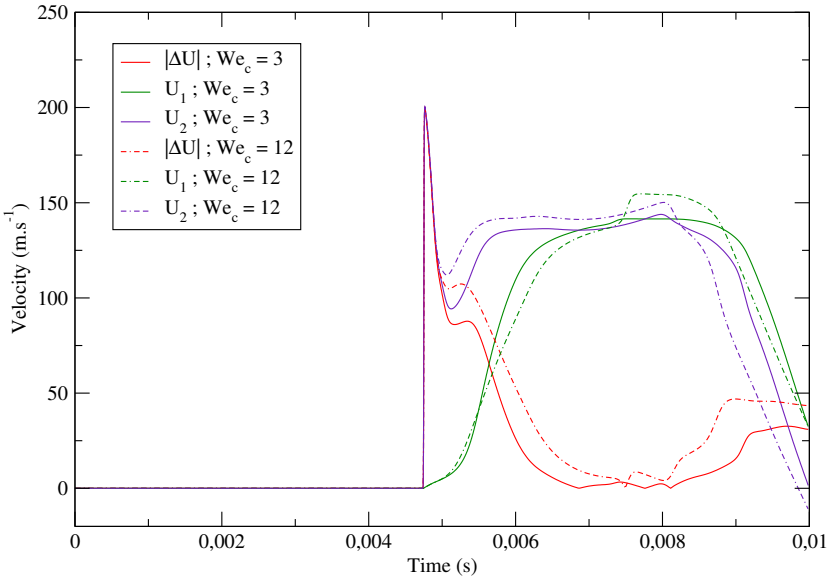

Figure 13: Chauvin experiment: evolution of the velocities at station 3 for a mesh of 20 000 cells. Index number 1 corresponds to the liquid phase and index number 2 corresponds to the gaseous phase.

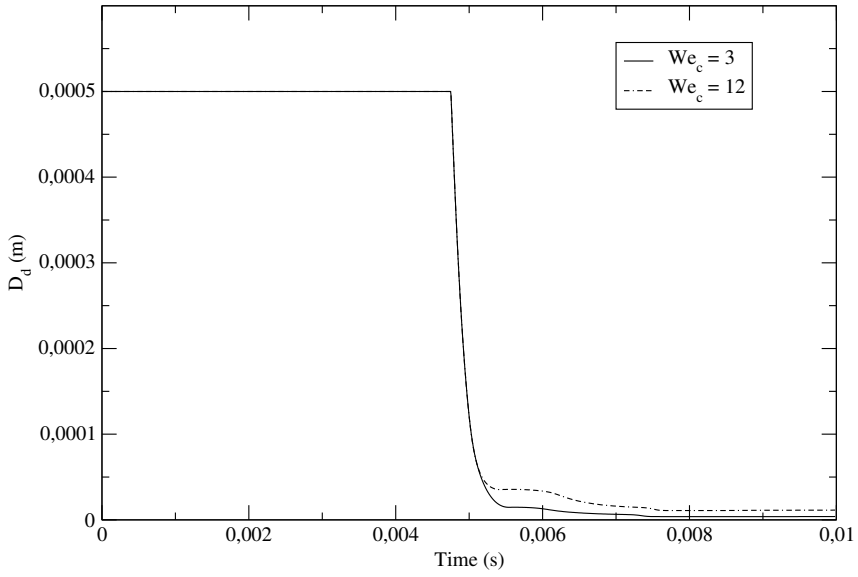

Figure 14: Chauvin experiment: evolution of the diameter D_d at station 3 for a mesh of 20 000 cells.

According to **Figure** 13, the velocity of the liquid phase (labelled one) and the gas phase (labelled two) are completely distinct, with a maximum gap of more than $200 m.s^{-1}$, right after the incident shock wave. The structural hypothesis of velocity disequilibrium between phases is thus retrieved in the numerical results. **Figure** 14 shows the impact of the value of the critical Weber number on the atomization process. Indeed, a

four times bigger critical Weber number results here in a twice larger droplet's diameter on the first plateau after the shock.

In **Appendix** 8, the Chauvin experiment [12] is also computed, assuming rigid particles, as conducted by authors in [11]. In that case, as the diameter of the droplets is constant, no pressure drop arises right after the incident shock wave, as expected (see **Figure** 3 of [11], and also [6]), even for a refined mesh.

2.2 Discrete source terms for a mixture of liquid water and vapour

As in the liquid-gas section, the velocity relaxation is taken into account before the thermodynamic part of the source terms.

2.2.1 Two algorithms for the simulation of the thermodynamic source terms

We recall that for $\Psi \in \{P, T, U\}$, $\Delta\Psi$ is set as:

$$\Delta\Psi = \Psi_l - \Psi_v \tag{127}$$

And for clarity, we note:

$$\Delta\mu = \frac{\mu_l}{T_l} - \frac{\mu_v}{T_v} \tag{128}$$

A- Fractional step approach

For a mixture of water and vapour, the relaxation effects, which are presented for a mixture of liquid and gas, must be complemented with the mass transfer terms. This fractional step scheme is thus composed of three steps, one for each thermodynamic effect. The sequence is as follows, still using the same time step Δt within each step:

$$\begin{aligned} \text{I:} \quad & W^n \xrightarrow{Pressure\ relaxation} W^{n*} \\ \text{II:} \quad & W^{n*} \xrightarrow{Heat\ transfer} W^{n*+} \\ \text{III:} \quad & W^{n*+} \xrightarrow{Mass\ transfer} W^{n+1} \end{aligned}$$

The first two steps are identical to the ones presented for a mixture of liquid and gas in **Section 2.1.1.A**. Besides, step III is taken from [18] and recalled in **Appendix 4**.

B- Coupled approach

Once more, the basic idea of this approach is to account for all the thermodynamic effects in one step.

First, the global system of source terms is recalled:

$$\begin{cases} \partial_t(\alpha_l) = K(W)\Delta P \\ \partial_t(m_l) = \Gamma_l(W) \\ \partial_t(m_l U_l) = \dfrac{U_l + U_v}{2}\Gamma_l(W) \\ \partial_t(\alpha_l E_l) + P_v \partial_t(\alpha_l) = \dfrac{U_l U_v}{2}\Gamma_l(W) - q(W)\Delta T \\ \partial_t(m_l + m_v) = 0 \\ \partial_t(m_l U_l + m_v U_v) = 0 \\ \partial_t(\alpha_l E_l + \alpha_v E_v) = 0 \end{cases} \tag{129}$$

From system (129), it can be obtained:

$$\begin{cases} \partial_t(\alpha_l) = K(W)\Delta P \\ \partial_t(m_l) = \Gamma_l(W) \\ \partial_t(m_l U_l) = \dfrac{U_l + U_v}{2}\Gamma_l(W) \\ \partial_t(m_l \epsilon_l) + P_v \partial_t(\alpha_l) = -q(W)\Delta T \\ \partial_t(m_l + m_v) = 0 \\ \partial_t(m_l U_l + m_v U_v) = 0 \\ \partial_t(\alpha_l E_l + \alpha_v E_v) = 0 \end{cases} \tag{130}$$

It can also be deduced from system (130) that:

$$\partial_t \left(m_l \epsilon_l + m_v \epsilon_v \right) = 0. \tag{131}$$

since:

$$\partial_t \left(m_l U_l^2 \right) = \frac{U_l U_v}{2} \Gamma_l = -\partial_t \left(m_v U_v^2 \right) \tag{132}$$

System (130) can be recast in two subsystems, which are:

$$\left\{ \begin{array}{l} \partial_t \left(\alpha_l \right) = K(W) \Delta P \\ \partial_t \left(m_l \right) = \Gamma_l \\ \partial_t \left(m_l \epsilon_l \right) = -P_v K(W) \Delta P - q(W) \Delta T \\ \partial_t (m_l + m_v) = 0 \\ \partial_t (m_l \epsilon_l + m_v \epsilon_v) = 0 \end{array} \right. \tag{133}$$

and:

$$\left\{ \begin{array}{l} \partial_t \left(m_l U_l \right) = \dfrac{U_l + U_v}{2} \Gamma_l \\ \partial_t (m_l U_l + m_v U_v) = 0 \end{array} \right. \tag{134}$$

System (133) can be solved first, independently of system (134).

From system (133), an equation of evolution for the thermodynamic quantity gaps can be derived, see [42]:

$$\partial_t \left(\begin{array}{c} \Delta P \\ \Delta T \\ \Delta \mu \end{array} \right) = -\mathscr{R}_{PT\mu} \left(\begin{array}{c} \Delta P \\ \Delta T \\ \Delta \mu \end{array} \right) \tag{135}$$

The coefficients of $\mathscr{R}_{PT\mu} \in \mathscr{M}_3(\mathbb{R})$ are detailed in [42] and recalled in **Appendix 5**.

Using an implicit Euler method, system (135) is discretized as follows:

$$\left(\begin{array}{c} \Delta P \\ \Delta T \\ \Delta \mu \end{array} \right)^{n+1} = (1 + \Delta t \mathscr{R}^n_{PT\mu})^{-1} \left(\begin{array}{c} \Delta P \\ \Delta T \\ \Delta \mu \end{array} \right)^{n} \tag{136}$$

The conservation laws included in (133) imply:

$$\left\{ \begin{array}{l} M_n = m_l^n + m_v^n = m_l^{n+1} + m_v^{n+1} \\ \xi_n = (m_l \epsilon_l)^n + (m_v \epsilon_v)^n = (m_l \epsilon_l)^{n+1} + (m_v \epsilon_v)^{n+1} \end{array} \right. \tag{137}$$

and the one included in (134) gives:

$$Q_n^U = (m_l U_l)^n + (m_v U_v)^n = (m_l U_l)^{n+1} + (m_v U_v)^{n+1} \tag{138}$$

Coupled (P-T,μ) relaxation algorithm:

Step 1: Compute ΔP^{n+1}, ΔT^{n+1} and $\Delta \mu^{n+1}$, solution of system (136). The matrix $\mathscr{R}_{PT\mu}$ is considered frozen at time t^n.

Step 2: Compute m_l^{n+1} as:

$$m_l^{n+1} = \frac{M_n}{1 + \frac{(M_n - m_l^n)}{m_l^n} \exp(\frac{\Delta \mu^{n+1}}{\tau_m^n \Gamma_0} \Delta t)} > 0 \tag{139}$$

Deduce $m_v^{n+1} = M_n - m_l^{n+1} > 0$ and set $\Gamma_l^{n+1} = \dfrac{m_l^{n+1} - m_l^n}{\Delta t}$.

Step 3: Compute P_l^{n+1} and T_l^{n+1}, solutions of the following system:

$$\left\{ \begin{array}{l} m_l^{n+1} \epsilon_l(P_l^{n+1}, T_l^{n+1}) + (M_n - m_l^{n+1}) \epsilon_v(P_l^{n+1} - \Delta P^{n+1}, T_l^{n+1} - \Delta T^{n+1}) = \xi_n \\ \dfrac{m_l^{n+1}}{\rho_l(P_l^{n+1}, T_l^{n+1})} + \dfrac{M_n - m_l^{n+1}}{\rho_v(P_l^{n+1} - \Delta P^{n+1}, T_l^{n+1} - \Delta T^{n+1})} = 1 \end{array} \right. \tag{140}$$

Step 4: Update P_v^{n+1}, T_v^{n+1}, α_l^{n+1} and α_v^{n+1} as:

$$\left\{\begin{array}{l} P_v^{n+1} = P_l^{n+1} - \Delta P^{n+1} \\ T_v^{n+1} = T_l^{n+1} - \Delta T^{n+1} \\ \alpha_l^{n+1} = \dfrac{m_l^{n+1}}{\rho_l(P_l^{n+1}, T_l^{n+1})} \\ \alpha_v^{n+1} = 1 - \alpha_l^{n+1} \end{array}\right. \tag{141}$$

Update ϵ_l^{n+1} and ϵ_v^{n+1} in agreement with (140).

Step 5: Then compute U_l^{n+1} and U_v^{n+1} solutions of:

$$\left\{\begin{array}{l} (m_l U_l)^{n+1} - (m_l U_l)^n = \Delta t \dfrac{\Gamma_l^{n+1}}{2}(U_l^{n+1} + U_v^{n+1}) \\ (m_v U_v)^{n+1} - (m_v U_v)^n = -\Delta t \dfrac{\Gamma_l^{n+1}}{2}(U_l^{n+1} + U_v^{n+1}) \end{array}\right. \tag{142}$$

Step 6: Update the total energies as:

$$\left\{\begin{array}{l} (\alpha_l E_l)^{n+1} = m_l^{n+1}\epsilon_l(P_l^{n+1}, T_l^{n+1}) + \dfrac{1}{2} m_l^{n+1}(U_l^{n+1})^2 \\ (\alpha_v E_v)^{n+1} = (\alpha_v E_v)^n + (\alpha_l E_l)^n - (\alpha_l E_l)^{n+1} \end{array}\right. \tag{143}$$

▫

Remark 4:

- Equation (139) is deduced from the mass conservation (133.2), with $\Delta\mu$ frozen at time t^{n+1}.
- System (140) is derived from the conservation law of the sum of the internal energies (131) and the immiscible constraint (1).
- System (142) is derived from system (134) by using an implicit Euler scheme.

Thus, we have:

Property 7: (Coupled P-T-μ algorithm)

- *System (142) is invertible whatever the time step is.*
- *If the three fundamentals minors of matrix $\mathscr{R}_{PT\mu}$ (135) are positive, then step 1 ensures the thermodynamic relaxation process over time, whatever the time step is.*
- *For a given couple of perfect gas EOS, solutions P_l^{n+1} and T_l^{n+1} of (140) in the admissible range, exist and are unique. Moreover, α_l^{n+1} belongs to [0,1] and the partial masses m_l^{n+1} and m_v^{n+1} remain positive.*

Proof. :

- Standard calculations give the determinant δ of system (142):

$$\delta = \frac{1}{2}(m_l^{n+1} m_v^n + m_l^n m_v^{n+1}). \tag{144}$$

  As δ is strictly positive whatever the time step is, system (142) is always invertible.

- System (140) is identical to (98), thus it benefits from the same properties.
- If the three fundamentals minors of $\mathscr{R}_{PT\mu}$ (135) are positive, then according to [42], **Lemma 1** applies and ensures the relaxation process over time, whatever the time step is.

□

2.2.2 Verification and comparison between the two approaches in a homogeneous case

In this section, the two schemes presented in the previous part are compared on different test cases. To do so, the flow is supposed to be homogeneous:

$$\forall \Psi(W),\ \partial_x \Psi(W) = 0 \tag{145}$$

and the velocities within each phase are assumed to be null. The different simulations are performed with time steps ranging between $10^{-10}\ s$ and $10^{-1}\ s$. All the relaxation time scales are supposed to be constant. Their values, the initial conditions and the coefficients of the EOS for the different cases are given in **Appendix 1**. Moreover, in order to ensure an effective relaxation time of each separated effect close to the relaxation time scale given by the user, the value of $\mathscr{P}_0$ and Γ_0 have to be set at $t = 0$ to:

$$\begin{cases} \mathscr{P}_0 = \| \alpha_v^0 \rho_l^0 (c_l^0)^2 + \alpha_l^0 \rho_v^0 (c_v^0)^2 - \alpha_v^0 \dfrac{\Delta P^0}{\rho_l^0 \left(\partial_{P_l}(\epsilon_l)|_{\rho_l}\right)^0} \| \\ \Gamma_0 = \| m_v^0 (\gamma_l C_{v_l} + \dfrac{\epsilon_{l_0}}{T_l^0}(2 + \dfrac{\epsilon_{l_0}}{C_{v_l} T_l^0}) + m_l^0 (\gamma_v C_{v_v} + \dfrac{\epsilon_{v_0}}{T_v^0}(2 + \dfrac{\epsilon_{v_0}}{C_{v_v} T_v^0}) \| \end{cases} \tag{146}$$

As it occurs in the liquid-gas framework, the fractional step algorithm can in some cases overestimate the pressure of the liquid phase for coarse time steps. For example, in case 3, (see **Figure** 15), using a time step of 10^{-3}s, the latter method leads to pressure values almost one hundred times bigger than the converged solution. For the same time stepping, the coupled algorithm overestimation is much lower (see **Figure** 16). Even if it is not the case here, the overestimation of the pressure P_l by the fractional step algorithm could lead to the violation of the relaxation conditions detailed in [42]. In addition, when case 3 is computed with a time step $\Delta t = 10^{-3} s$, the fractional step algorithm is unable to return to pressure equilibrium, and even stops just before $t = 0.02 s$ (see **Figure** 17). The temperature profiles of the liquid water and vapour, computed with the fractional step algorithm and the coupled algorithm, are given in **Figures** 19 and 20 respectively.

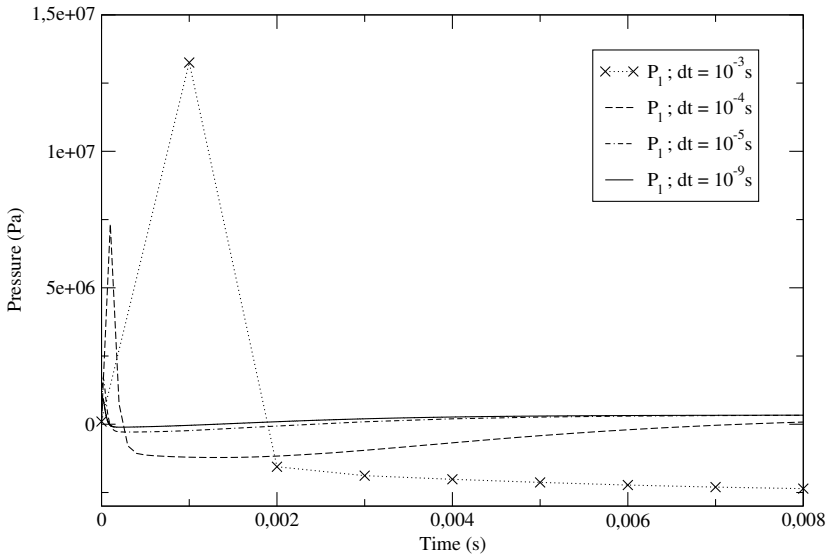

Figure 15: Evolution of P_l in case 3 computed with the fractional step algorithm. $\tau_P = 10^{-5} s$, $\tau_T = 10^{-4} s$, $\tau_m = 10^{-6} s$. The initial conditions are given in **Appendix 1**.

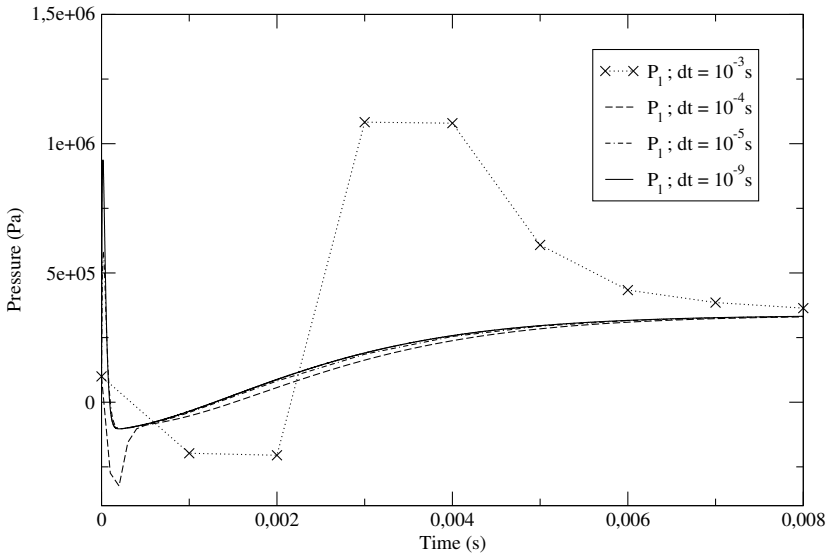

Figure 16: Evolution of P_l in case 3 computed with the coupled algorithm. $\tau_P = 10^{-5}s$, $\tau_T = 10^{-4}s$, $\tau_m = 10^{-6}s$. The initial conditions are given in **Appendix 1**.

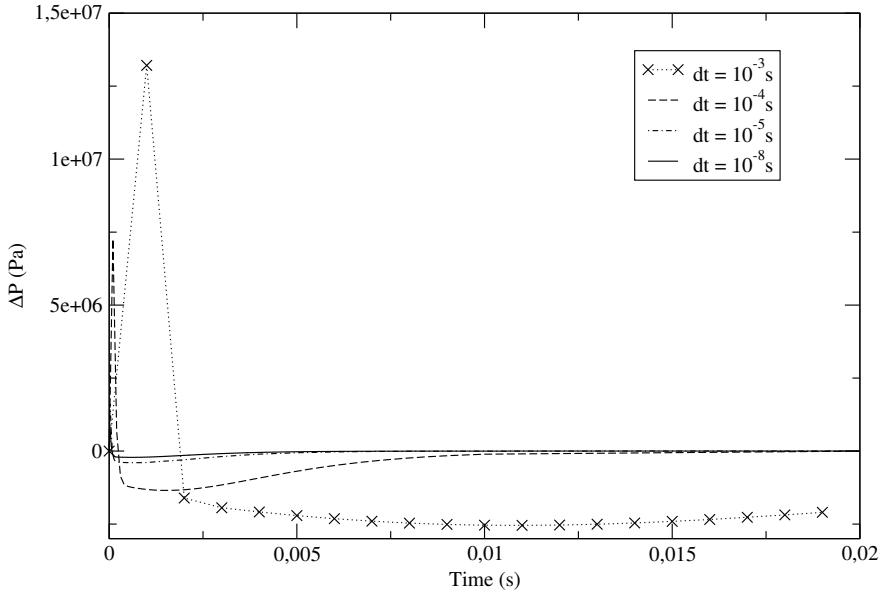

Figure 17: Evolution of ΔP in case 3 computed with the fractional step algorithm. $\tau_P = 10^{-5}s$, $\tau_T = 10^{-4}s$, $\tau_m = 10^{-6}s$. The initial conditions are given in **Appendix 1**.

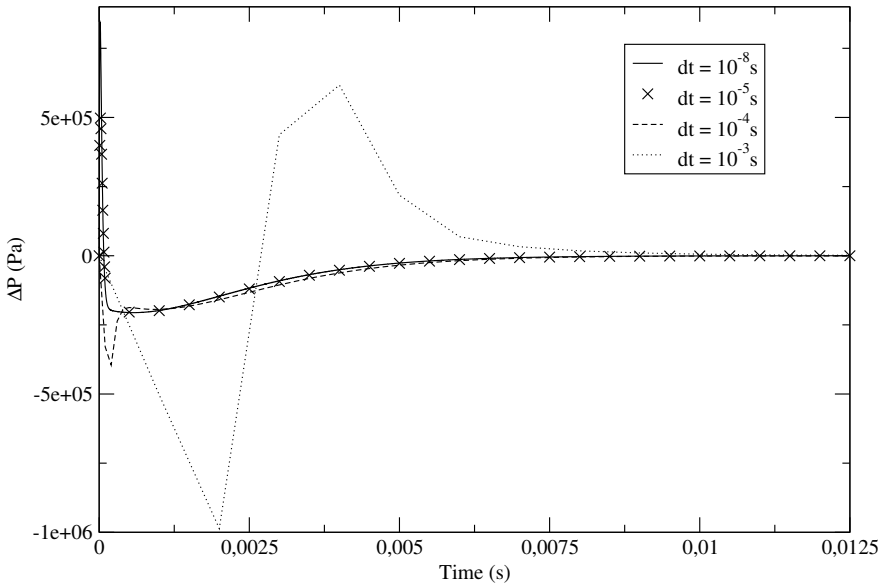

Figure 18: Evolution of ΔP in case 3 computed with the coupled algorithm. $\tau_P = 10^{-5}s$, $\tau_T = 10^{-4}s$, $\tau_m = 10^{-6}s$. The initial conditions are given in **Appendix 1**.

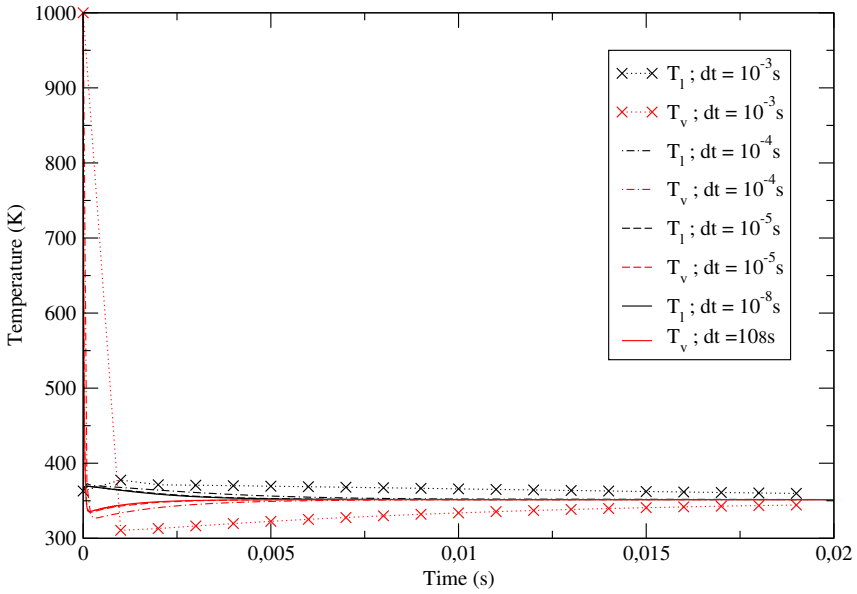

Figure 19: Evolution of T_l and T_v in case 3 computed with the fractional step algorithm. $\tau_P = 10^{-5}s$, $\tau_T = 10^{-4}s$, $\tau_m = 10^{-6}s$. The initial conditions are given in **Appendix 1**.

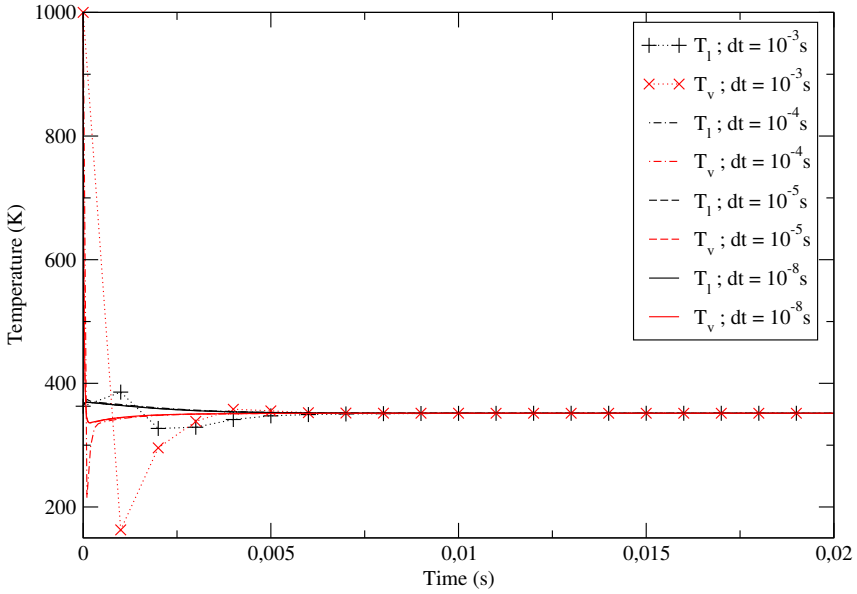

Figure 20: Evolution of T_l and T_v in case 3 computed with the coupled algorithm. $\tau_P = 10^{-5}s$, $\tau_T = 10^{-4}s$, $\tau_m = 10^{-6}s$. The initial conditions are given in **Appendix 1**.

A convergence study is presented below. The error $E_\Psi(t, \Delta t)$ is defined as in the liquid gas section (117). The speed of convergence is close to one (see **Figure** 21) for the two approaches, as expected. Note that

the value of the error for the fractional step algorithm is about one hundred times bigger for the pressure P_l than the one obtained with the coupled algorithm.

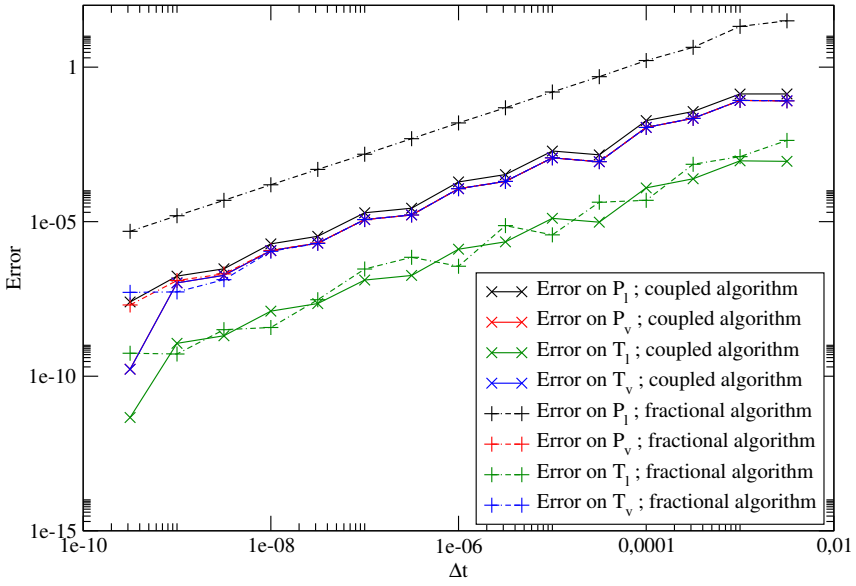

Figure 21: Homogeneous case: Convergence curve for case 2: $\tau_P = 10^{-5}s$, $\tau_T = 10^{-3}s$, $\tau_m = 5.\ 10^{-3}s$. The initial conditions are given in **Appendix 1**

Besides, the ratio of computational costs is in the range $[5, 12]$ in favour of the coupled algorithm, for a given Δt, see **Table** 2. Moreover, as mentioned before, the fractional step algorithm even blows up on coarse meshes.

dt	Coupled algorithm	Fractional algorithm
$10^{-2}s$	$1.28\ 10^{-7}$	Blows up
$10^{-4}s$	$5.8\ 10^{-7}$	$2.71\ 10^{-6}$
$10^{-6}s$	$1.29\ 10^{-5}$	$1.16\ 10^{-4}$
$10^{-8}s$	$8.64\ 10^{-4}$	$9.90\ 10^{-3}$
$10^{-10}s$	$8.03\ 10^{-2}$	1

Table 2: CPU normalised by the CPU of the fractional step algorithm using $\Delta t = 10^{-10}s$ for case 3

2.2.3 Application: One dimensional shock tube in vapour with a cloud of water droplets

The aim of this section is to test the coupled algorithm for a mixture of liquid water and its vapour. The application test case is composed of a one dimensional shock tube in vapour. At $t = 0$, a cloud of water droplets lies inside a portion of the tube. The initial conditions along the tube are set as follows:

Abscissa interval (m)	α_l	P_l (bar)	P_v (bar)	T_l (K)	T_v (K)
$x \in [0.00, 0.75]$	10^{-8}	6	6	1000	1000
$x \in [0.75, 3.00[\cup]3.40, 3.75]$	10^{-8}	1	1	1000	1000
$x \in [3.00, 3.40]$	0.03	1	1	293	1000

Three probes are set inside the tube:

- S_1 is located inside the initial vapour layer of the tube: $x = 1.77m$
- S_2 is located at the beginning of the initial cloud of water droplets: $x = 3.08m$
- S_3 is located in the middle of the initial zone of liquid - vapour mixture: $x = 3.20m$

Relaxation time scales and EOS coefficients are the same as those used for the convergence curves in **Figure** 21 and can be found in **Appendix 1**, case 2. In this test case, the particles are supposed to be rigid.

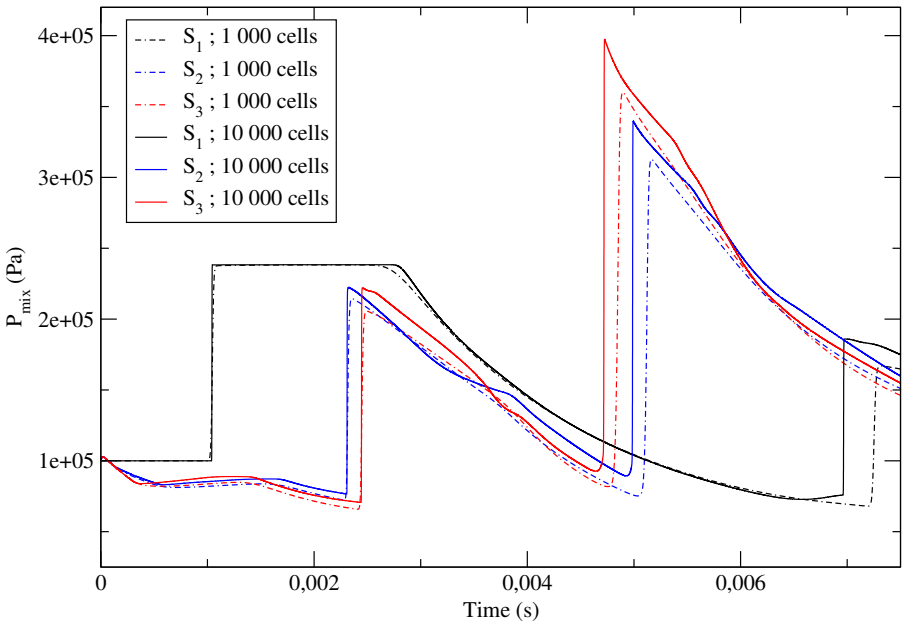

Figure 22: Evolution of P_{mix} for two meshes including 1 000 cells and 10 000 cells

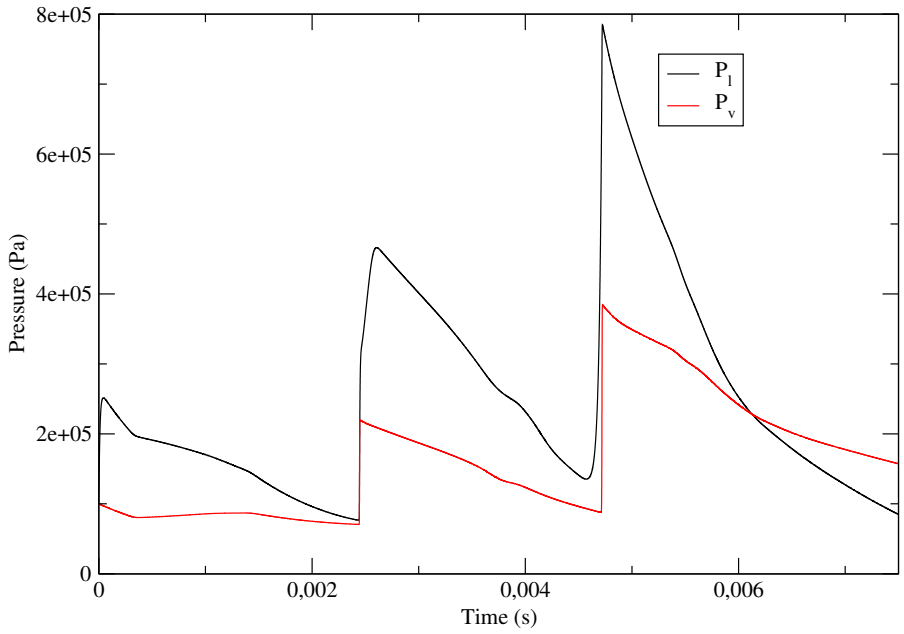

Figure 23: Evolution of P_l and P_v at station 3 with the initial condition of case 2. A mesh of 10 000 cells has been used.

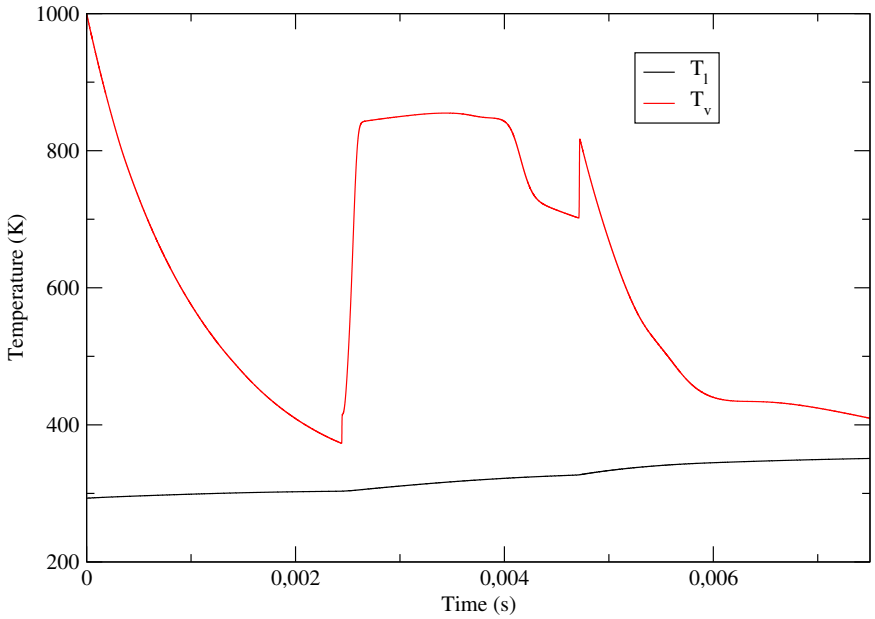

Figure 24: Evolution of T_l and T_v at station 3 with the initial condition of case 2. A mesh of 10 000 cells has been used.

As expected, the solution obtained in the homogeneous case is retrieved at station 3 in the first time steps, see **Figures** 22, 23 and 24. Moreover, in this case, the pressure disequilibrium is substantial as ΔP can be four times larger than the initial pressure, see **Figure** 23. The temperature disequilibrium is also significant, as it is still about 70% of its initial value after the shock wave. The difference of velocities ΔU is also quite large, close to 600 $m.s^{-1}$ right after the shock wave.

Remark 5: Eventually, it is also worth noting that the fractional step algorithm fails to compute an approximate solution of this test case.

3 Conclusion:

When focusing on the class of liquid-gas flow models considered here, conditions (43), (44) and (45) are the true conditions that guarantee the effective relaxation process. For most EOS, conditions (44) and (45) are not trivial and have to be numerically tested inside the code. In most cases, conditions (44) and (45) also involve initial conditions. For liquid-vapour flows, four conditions arise, which also involve EOS and initial conditions.

The coupled algorithm, which has been introduced for the treatment of the sub-system associated with the source terms (34), is grounded on the analysis of relaxation effects. This new strategy has been compared with the classical fractional step method. The comparison is clearly in favour of the coupled algorithm, as it was expected, and this is particularly true when rather coarse time steps are considered, or equivalently on coarse "industrial" meshes. Indeed, the coupled algorithm is more stable, especially in the liquid-vapour case. The latter algorithm also provides a higher accuracy for a given mesh size, and a lower computational cost for a comparable accuracy, than the fractional step approach. Moreover, some particular test cases exhibit a rather strange behaviour of the fractional approach, and this might in some sense be compared with what happens when computing shallow-water equations with well-balanced schemes versus the fractional step method. It also clearly arises that mass transfer terms have a huge impact on the practical stability of the whole algorithm.

In addition, substantial values of ΔU, ΔP and ΔT can be observed in the transient regime throughout this paper, which pleads against any hypothesis of instantaneous return-to-equilibrium, for both mechanical and thermodynamic quantities. *A posteriori*, it also justifies the investigation of the relaxation process.

Of course, higher-order time schemes, such as the Radau V method presented in [65], might be used to improve the accuracy of the coupled algorithm, but this lies beyond the scope of the present work. Eventually, relaxation solvers such as those presented in [14] and [9] could improve both the accuracy and the computational cost when accounting for convective terms (61).

Acknowledgments:

The second author has benefited from partial financial support by ANRT under CIFRE grant 2020/0946. Both authors would like to thank the reviewers for their useful comments and suggestions. All computational facilities were provided by EDF.

References

[1] Grégoire Allaire, Sébastien Clerc, and Samuel Kokh. A five-equation model for the numerical simulation of interfaces in two-phase flows. Comptes Rendus de l'Académie des Sciences-Series I-Mathematics, 331(12):1017–1022, 2000.

[2] Annalisa Ambroso, Christophe Chalons, and Pierre-Arnaud Raviart. A Godunov-type method for the seven-equation model of compressible two-phase flow. Computers & Fluids, 54:67–91, 2012.

[3] Melvin R. Baer and Jace W. Nunziato. A two phase mixture theory for the deflagration to detonation transition (DDT) in reactive granular materials. Int. J. Multiphase Flow, 12-6:861–889, 1986.

[4] Zbigniew Bilicki and Joseph Kestin. Physical aspects of the relaxation model in two-phase flow. Proceedings of the Royal Society of London. A. Mathematical and Physical Sciences, 428(1875):379–397, 1990.

[5] Hamza Boukili and Jean-Marc Hérard. Relaxation and simulation of a barotropic three-phase flow model. ESAIM: Math. Modeling and Numerical Analysis, 53:1031–1059, 2019.

[6] Hamza Boukili and Jean-Marc Hérard. Simulation and preliminary validation of a three-phase flow model with energy. Computers and Fluids, 221:104868, 2021.

[7] Didier Bresch and Matthieu Hillairet. Note on the derivation of multi-component flow systems. Proc. Am. Math. Soc., 143:3429–3443, 2015.

[8] Didier Bresch and Matthieu Hillairet. A compressible multifluid system with new physical relaxation terms. Annales scientifiques de l' Ecole Normale Supérieure, 2016.

[9] Jean Bussac and Khaled Saleh. Numerical simulation of a barotropic two-phase flow model with miscible phases. To appear in Springer proceedings of FVCA-10 conference, 2023.

[10] Alice Chauvin. Etude experimentale de l'attenuation d'une onde de choc par un nuage de gouttes et validation numerique. PhD thesis, Université Aix-Marseille, 2012. Available at : https://www.theses.fr/2012AIXM4732.pdf.

[11] Alice Chauvin, Eric Daniel, Ashwin Chinnayya, Jacques Massoni, and Georges Jourdan. Shock waves in sprays: numerical study of secondary atomization and experimental comparison. Shock Waves, 26:403–415, 2016.

[12] Alice Chauvin, Georges Jourdan, Eric Daniel, Lazhar Houas, and Robert Tosello. Experimental investigation of the propagation of a planar shock wave through a two-phase gas-liquid medium. Physics of fluids, 23(11):113301, 2011.

[13] Frédéric Coquel, Thierry Gallouët, Jean-Marc Hérard, and Nicolas Seguin. Closure laws for a two fluid two-pressure model. Comptes Rendus Académie des Sciences Paris, I-332:927–932, 2002.

[14] Frédéric Coquel, Jean-Marc Hérard, and Khaled Saleh. A positive and entropy-satisfying finite volume scheme for the Baer–Nunziato model. Journal of Computational Physics, 330:401–435, 2017.

[15] Frédéric Coquel, Jean-Marc Hérard, Khaled Saleh, and Nicolas Seguin. A robust entropy- satisfying finite volume scheme for the isentropic Baer – Nunziato model. ESAIM: Mathematical Modelling and Numerical Analysis, 48(1):165–206, 2014.

[16] Frédéric Coquel, Jean-Marc Hérard, Khaled Saleh, and Nicolas Seguin. Two properties of two-velocity two-pressure models for two-phase flows. Communications in Mathematical Sciences, 12:593–600, 2014.

[17] Fréderic Coquel, Claude Marmignon, Pratik Rai, and Florent Renac. An entropy stable high-order discontinuous galerkin spectral element method for the Baer–Nunziato two-phase flow model. Journal of Computational Physics, 431:110135, 2021.

[18] Fabien Crouzet, Frédéric Daude, Pascal Galon, Jean-Marc Hérard, Olivier Hurisse, and Yujie Liu. Validation of a two-fluid model on unsteady liquid-vapor water flows. Computers and Fluids, 119:131–142, 2015.

[19] P. Downar-Zapolski, Zbigniew Bilicki, Léon Bolle, and J. Franco. The non-equilibrium relaxation model for one-dimensional flashing liquid flow. International journal of multiphase flow, 22(3):473–483, 1996.

[20] Pedro Embid and Melvin R. Baer. Mathematical analysis of a two-phase continuum mixture theory. Continuum Mechanics and Thermodynamics, 4:279–312, 1992.

[21] Robert Eymard, Thierry Gallouët, and Raphaèle Herbin. Finite volume methods. Handbook of numerical analysis, 7:713–1018, 2000.

[22] Gloria Faccanoni, Samuel Kokh, and Grégoire Allaire. Approximation of liquid–vapor phase transition for compressible fluids with tabulated EoS. Comptes Rendus Mathematique, 348(7-8):473–478, 2010.

[23] Tore Flåtten and Gaute Linga. A hierarchy of non-equilibrium two-phase flow models. ESAIM: Proceedings and Surveys, 66:109–143, 2019.

[24] Tore Flåtten and Halvor Lund. Relaxation two-phase flow models and the sub-characteristic condition. Mathematical Models and Methods in Applied Sciences, 21:2379–2407, 2011.

[25] Thierry Gallouët, Philippe Helluy, Jean-Marc Hérard, and Julien Nussbaum. Hyperbolic relaxation models for granular flows. Mathematical Modeling and Numerical Analysis, 44:371–400, 2010.

[26] Thierry Gallouët, Jean-Marc Hérard, and Nicolas Seguin. Numerical modeling of two-phase flows using the two fluid two-pressure approach. Math. Models Methods in Applied Sciences, 14:663–700, 2004.

[27] Sergey Gavrilyuk. Multiphase flow modeling via Hamilton's principle. Variational models and methods in solid and fluid mechanics, pages 163–210, 2011.

[28] Sergey Gavrilyuk. The structure of pressure relaxation terms: the one-velocity case. EDF report H-I83-2014-0276-EN, 2014. Available upon request to: sergey.gavrilyuk@univ-amu.fr.

[29] Sergey Gavrilyuk, Henri Gouin, and Yurii Perepechko. A variational principle for two fluid models. Comptes Rendus Académie Sciences Paris, IIb-324:483–490, 1997.

[30] Sergey Gavrilyuk and Richard Saurel. Mathematical and numerical modeling of two-phase compressible flows with micro-inertia. Journal of Computational Physics, 175:326–360, 2002.

[31] Boris E. Gelfand. Droplet breakup phenomena in flows with velocity lag. Progress in energy and combustion science, 22(3):201–265, 1996.

[32] James Glimm, David Saltz, and David H. Sharp. Two phase flow modelling of a fluid mixing layer. Journal of Fluid Mechanics, 378:39–47, 1999.

[33] Edwige Godlewski and Pierre-Arnaud Raviart. Numerical approximation of hyperbolic systems of conservation laws, volume 118. Springer Science & Business Media, 2013.

[34] Lene Grabowsky, Maren Hantke, and Siegfried Müller. News on Baer–Nunziato type model at pressure equilibrium. Continuum Mechanics and Thermodynamics, 33:767–788, 2021.

[35] Vincent Guillemaud. Modelisation et simulation numerique des ecoulements diphasiques par une approche bifluide a deux pressions. PhD thesis, Université Aix-Marseille, 2007. Available at : https://tel.archives-ouvertes.fr/tel-00169178v1.

[36] Ee Han, Maren Hantke, and Siegfried Müller. Efficient and robust relaxation procedures for multi-component mixtures including phase transition. Journal of Computational Physics, 338, 2017.

[37] Maren Hantke and Siegfried Müller. Analysis and simulation of a new multi-component two-phase flow model with phase transition and chemical reactions. Quarterly of Applied Mathematics, 76, 2018.

[38] Maren Hantke, Siegfried Müller, and Pascal Richter. Closure conditions for non-equilibrium multi-component models. Continuum Mechanics and Thermodynamics, 28:1157–1189, 2016.

[39] Philippe Helluy. Simulation numérique des écoulements multiphasiques: de la théorie aux applications. Habilitation à diriger des recherches, Université du Sud Toulon Var, January 2005. Available at https://tel.archives-ouvertes.fr/tel-00657839/file/habilitation-helluy.pdf.

[40] Jean-Marc Hérard. A three-phase flow model. Mathematical and Computer Modeling, 45:732–755, 2007.

[41] Jean-Marc Hérard. A class of compressible multiphase flow models. Comptes Rendus Mathématique, 354:954–959, 2016.

[42] Jean-Marc Hérard. The relaxation process in a class of two-phase flow models. internal EDF report 6125-3016-2022-00089-EN, 2022. Available upon request to: jean-marc.herard@edf.fr.

[43] Jean-Marc Hérard and Guillaume Jomée. Pressure relaxation in some multiphase flow models. ESAIM: Proceedings and surveys, 72:19–40, 2023. https://hal.science/hal-03241934v2.

[44] Matthieu Hillairet. On Baer–Nunziato multiphase flow models. ESAIM: Proceedings and surveys, 66:61–83, 2019.

[45] Olivier Hurisse. Simulation des écoulements industriels diphasiques compressibles. Habilitation à diriger des recherches, Université de Strasbourg, July 2017. Available at : https://hal.archives-ouvertes.fr/tel-01570985/file/hdr-hurisse.pdf.

[46] Mamoru Ishii. Thermo-fluid dynamic theory of two-phase flow. Eyrolles-Collection de la Direction des Etudes et Recherches EDF, 1975.

[47] Stéphane Jaouen. Etude mathématique et numérique de stabilité pour des modeles hydrodynamiques avec transition de phase. PhD thesis, Paris 6, 2001.

[48] Ashwani Kapila, Steven F. Son, John B. Bdzil, Ralph Menikoff, and Donald S. Stewart. Two phase modeling of a DDT: structure of the velocity relaxation zone. Physics of Fluids, 9-12:3885–3897, 1997.

[49] Mathieu Labois. Modélisation des déséquilibres mécaniques pour les écoulements diphasiques. Approche par relaxation et par modèle réduit. PhD thesis, Université Aix-Marseille, 2008. Available at https://tel.archives-ouvertes.fr/tel-00338818v1.

[50] Olivier Le Métayer and Richerd Saurel. The Noble-Abel stiffened-gas equation of state. Physics of Fluids, 28, 2016.

[51] Halvor Lund. A hierarchy of relaxation models for two-phase flow. SIAM Journal on Applied Mathematics, 72:1713–1741, 2012.

[52] Marica Pelanti. Arbitrary-rate relaxation techniques for the numerical modeling of compressible two-phase flows with heat and mass transfer. International Journal of Multiphase Flow, 153, 2022.

[53] Marica Pelanti and Keh-Ming Shyue. A numerical model for multiphase liquid–vapor–gas flows with interfaces and cavitation. International Journal of Multiphase Flow, 113, 2019.

[54] Stéphane Picchi. MC3D Version 3.9 : Description of the models of the premixing application. IRSN internal report, 2017.

[55] Pratik Rai. Modeling and numerical simulation of compressible multicomponent flows. PhD thesis, Institut Polytechnique de Paris, 2021. Available at : https://tel.archives-ouvertes.fr/tel-03461287.

[56] Barbara Re and Rémi Abgrall. A pressure-based method for weakly compressible two-phase flows under a Baer–Nunziato type model with generic equations of state and pressure and velocity disequilibrium. International Journal for Numerical Methods in Fluids, 2022.

[57] Vladimir Vasil'evich Rusanov. Calculation of interaction of non-steady shock waves with obstacles. NRC, Division of Mechanical Engineering, 1962.

[58] Khaled Saleh. Analyse et Simulation Numérique par Relaxation d'Ecoulements Diphasiques Compressibles. Contributio Theses, Université Pierre et Marie Curie - Paris VI, December 2012. Available at https://tel.archives-ouvertes.fr/tel-00761099/file/These_KhaledSaleh.pdf.

[59] Khaled Saleh. A relaxation scheme for a hyperbolic multiphase flow model-part i: Barotropic eos. ESAIM: Mathematical Modelling and Numerical Analysis, 53(5):1763–1795, 2019.

[60] Richard Saurel and Rémi Abgrall. A multiphase Godunov method for compressible multifluid and multiphase flows. J. of Computational Physics, 150:425–467, 1999.

[61] Donald W. Schwendeman, Christopher W. Wahle, and Ashwana K. Kapila. The Riemann problem and a high-resolution Godunov method for a model of compressible two-phase flow. Journal of Computational Physics, 212(2):490–526, 2006.

[62] Mai D. Thanh, Dietmar Kröner, and Nguyen T. Nam. Numerical approximation for a Baer–Nunziato model of two-phase flows. Applied Numerical Mathematics, 61(5):702–721, 2011.

[63] Mai D. Thanh and Duong X. Vinh. The Riemann problem for the nonisentropic Baer–Nunziato model of two-phase flows. Nonlinear Analysis: Real World Applications, 67:103623, 2022.

[64] Svetlana A. Tokareva and Eleuterio F. Toro. HLLC-type Riemann solver for the Baer–Nunziato equations of compressible two-phase flow. Journal of Computational Physics, 229(10):3573–3604, 2010.

[65] Gerhard Wanner and Ernst Hairer. Solving ordinary differential equations II, volume 375. Springer Berlin Heidelberg, 1996.

Appendix 1: Numerical parameters

Homogeneous flow: liquid-gas

	Case 1	Case 5
τ_P	10^{-5}s	10^{-5}s
τ_T	10^{-3}s	5.10^{-5}s
α_l	0.3	0.03
P_l(t=0)	10^5Pa	10^5Pa
P_g(t=0)	10^5Pa	10^5Pa
T_l(t=0)	363 K	2500 K
T_g(t=0)	1000 K	363 K

Table 3: Simulation parameters for the homogeneous liquid gas cases and initial conditions

	Case 1	Case 5
γ_l	1.614924811807376e+00	2.2838590974110350e+01
γ_g	1.085507894797296e+00	1.614924811807376e+00
C_{v_l}	1.452904592629688e+03	1.2872948262582229e+01
C_{v_g}	4.441148752333071e+03	1.452904592629688e+03
$\hat{\Pi}_l$	3.563521398523755e+08	1.8847923625716622e+09
$\hat{\Pi}_g$	0.0	3.563521398523755e+08
ϵ_{l_0}	0.0	-1.3316200000000000e+05
ϵ_{g_0}	0.0	0.0
s_{l_0}	0.0	0.0
s_{g_0}	-4.769786773517021e+04	0.0

Table 4: EOS for the homogeneous liquid gas cases

Shock Tube Chauvin [12]

	Chauvin experiment
γ_l	27.07619047619048
γ_g	1.4
C_{v_l}	10.58283017395257e
C_{v_g}	717.142857143e
$\hat{\Pi}_l$	8.063584804783680 $.10^7$
$\hat{\Pi}_g$	0.0
ϵ_{l_0}	0.0
ϵ_{g_0}	0.0
s_{l_0}	0.0
s_{g_0}	0.0

Table 5: EOS for the Chauvin experiment [10]

Liquid-vapour

	Case 3	Case 2
τ_P	$10^{-5}s$	10^{-5}s
τ_T	$10^{-4}s$	10^{-3}s
τ_m	$10^{-6}s$	5.10^{-3}s
α_l	0.03	0.03
P_l(t=0)	10^5Pa	10^5Pa
P_v(t=0)	10^5Pa	10^5Pa
T_l(t=0)	363 K	293 K
T_g(t=0)	1000 K	1000 K

Table 6: Numerical parameters for the liquid gas simulations and initial conditions

γ_l	1.614924811807376e+00
γ_g	1.085507894797296e+00
C_{v_l}	1.452904592629688e+03
C_{v_g}	4.441148752333071e+03
$\hat{\Pi}_l$	3.563521398523755e+08
$\hat{\Pi}_g$	0.0
ϵ_{l_0}	0.0
ϵ_{g_0}	0.0
s_{l_0}	0.0
s_{g_0}	-4.769786773517021e+04

Table 7: EOS for all the liquid vapour simulations

Appendix 2: Velocity relaxation algorithm

During this step, system (5) become, for $k \in \{g, v\}$:

$$\begin{cases} \partial_t \alpha_l = 0 \\ \partial_t m_l = 0 \\ m_l \partial_t U_l = -d(W)\Delta U \\ \partial_t \left(\alpha_l E_l\right) = -d(W)\dfrac{U_l + U_k}{2}\Delta U \\ \partial_t \left(m_l + m_k\right) = 0 \\ \partial_t \left(m_l U_l + m_k U_k\right) = 0 \\ \partial_t \left(\alpha_l E_l + \alpha_k E_k\right) = 0 \end{cases} \tag{147}$$

The following algorithm is taken from [26]:

Velocity relaxation algorithm:

Step 1: Compute U_l^{n+1-} and U_k^{n+1-} as:

$$\begin{cases} U_l^{n+1-} = U_l^{n+1*} - \Delta U^{n+1*} \dfrac{m_k^{n+1*}\left(1 - e^{-\frac{\Delta t}{\tau_U^{n+1*}}}\right)}{m_k^{n+1*} + m_l^{n+1*}} \\ U_k^{n+1-} = U_l^{n+1*} + \Delta U^{n+1*} \dfrac{m_l^{n+1*}\left(1 - e^{-\frac{\Delta t}{\tau_U^{n+1*}}}\right)}{m_k^{n+1*} + m_l^{n+1*}} \end{cases} \tag{148}$$

Step 2: Compute $(m_l\epsilon_l)^{n+1-}$ and $(m_k\epsilon_k)^{n+1-}$ as:

$$\begin{cases} (m_l\epsilon_l)^{n+1-} = (m_l\epsilon_l)^{n+1*} + \dfrac{m_l^{n+1*}m_k^{n+1*}}{m_l^{n+1*}+m_k^{n+1*}}\dfrac{\left(\Delta U^{n+1*}\right)^2}{2}\left(1-e^{-\frac{2\Delta t}{\tau_U^{n+1*}}}\right) \\ (m_k\epsilon_k)^{n+1-} = (m_k\epsilon_k)^{n+1*} \end{cases} \tag{149}$$

Step 3: Update the total energies as:

$$\begin{cases} (\alpha_l E_l)^{n+1-} = (m_l\epsilon_l)^{n+1-} + \dfrac{1}{2}m_l^{n+1*}(U_l^{n+1-})^2 \\ (\alpha_k E_k)^{n+1-} = (\alpha_k E_k)^{n+1*} + (\alpha_l E_l)^{n+1*} - (\alpha_l E_l)^{n+1-} \end{cases} \tag{150}$$

□

Appendix 3: Interfacial area

The definition of the interfacial area of the water phase is recalled:

$$\mathscr{A} = \frac{6\alpha_l}{D_d} \tag{151}$$

Its equation of evolution is supposed to be:

$$\frac{\partial \mathscr{A}}{\partial t} + \nabla(\mathscr{A}U_l) = g(\mathscr{A}, W); \tag{152}$$

with:

$$g(\mathscr{A}, W) = C_0\frac{\mathscr{A}^2}{6\alpha_l}(\frac{\rho_l}{\rho_g})^{1/2}U_r f(We); \tag{153}$$

with $U_r = \|U_l - U_g\|$ and We the Weber number define as follows:

$$We = \frac{\rho_l U_r^2 D_d}{\sigma_d} \tag{154}$$

with $\sigma_d = 73\ .10^{-3}(N.m^{-1})$ a reference surface tension [54] . Moreover f(We) is defined as:

$$f(We) = 1\ ,\ if\ \ We > We_c\ ;\ f(We) = 0\ otherwise \tag{155}$$

where We_c is called the critical Weber.

Adding this new equation does not change the structure and properties of the global system (5) according to [5]. Hence, it is chosen for the simulation. The numerical scheme used to simulate (152) is detailed in [5]. It consists of a fractional step method, splitting the convective part and the source term part. Those two steps will respectively be inserted inside the explicit simulation step of the convective part of system (5) and the implicit simulation of the source terms of the same system.

Appendix 4: Mass transfer algorithm

During this step, system (5) writes as:

$$\begin{cases} \partial_t \alpha_v = 0 \\ \partial_t m_v = \Gamma_v \\ \partial_t (m_v U_v) = \dfrac{U_l + U_v}{2} \Gamma_v \\ \partial_t \left(\alpha_v E_v\right) = \dfrac{U_l U_k}{2} \Gamma_v \\ \partial_t \left(m_l + m_v\right) = 0 \\ \partial_t \left(m_l U_l + m_v U_v\right) = 0 \\ \partial_t \left(\alpha_l E_l + \alpha_v E_v\right) = 0 \end{cases} \tag{156}$$

with:

$$\Gamma_v = \frac{1}{\Gamma_0 \tau_m} \frac{m_l m_g}{m_l + m_g} \Delta\mu \tag{157}$$

From (156), a conservation law of the internal energies is obtained during this step:

$$\begin{cases} \partial_t \left(m_v \epsilon_v\right) = 0 \\ \partial_t \left(m_l \epsilon_l\right) = 0 \end{cases} \tag{158}$$

which implies that:

$$\Gamma_v = \tilde{\Gamma}_v(m_l) \tag{159}$$

The following algorithm is taken from [18]. A detailed version in French is also available in [45]:

Mass transfer algorithm:

Step 1: Compute m_l^{n+1*}, solution of:

$$m_l^{n+1*} = m_l^{n*} - \Delta t \Gamma_v(m_l^{n+1*}) \tag{160}$$

and update $m_v^{n+1*} = m_l^{n*} + m_v^{n*} - m_l^{n+1*}$.

Step 2: Compute U_l^{n+1*} and U_v^{n+1*} as:

$$\begin{cases} (m_l U_l)^{n+1*} = (m_l U_l)^{n*} - \Delta t \Gamma_l (m_l^{n+1*})^{n+1} \dfrac{U_l^{n+1*} + U_v^{n+1*}}{2} \\ (m_v U_v)^{n+1*} = (m_v U_v)^{n*} + (m_l U_l)^{n*} - (m_l U_l)^{n+1*} \end{cases} \tag{161}$$

Step 3: Update the total energies as:

$$\begin{cases} (\alpha_l E_l)^{n+1*} = (\alpha_l E_l)^{n*} - \Delta t \Gamma_l (m_l^{n+1*})^{n+1} \dfrac{U_l^{n+1*} U_v^{n+1*}}{2} \\ (\alpha_v E_v)^{n+1*} = (\alpha_v E_v)^{n*} + (\alpha_l E_l)^{n*} - (\alpha_l E_l)^{n+1*} \end{cases} \tag{162}$$

□

Appendix 5: Coefficients of the matrix $\mathscr{R}_{PT\mu}$

Matrix $\mathscr{R}_{PT\mu}(W) \in R_{3\times 3}$ is as follow, see [42]:

$$\mathscr{R}_{PT\mu}(W) = \begin{pmatrix} a^{lv}_{PP}(W) & a^{lv}_{PT}(W) & a^{lv}_{P\mu}(W) \\ a^{lv}_{TP}(W) & a^{lv}_{TT}(W) & a^{lv}_{T\mu}(W) \\ a^{lv}_{\mu P}(W) & a^{lv}_{\mu T}(W) & a^{lv}_{\mu\mu}(W) \end{pmatrix} \tag{163}$$

The above mentioned coefficients are as follows:

$$\begin{cases} a^{lv}_{PP}(W) = K(W)\left(A_l + A_v - \dfrac{\Delta P}{m_l \partial_{P_l}(\epsilon_l)\,|_{\rho_l}}\right) , \\ a^{lv}_{PT}(W) = q(W)\left(\dfrac{1}{m_l \partial_{P_l}(\epsilon_l)\,|_{\rho_l}} + \dfrac{1}{m_v \partial_{P_v}(\epsilon_v)\,|_{\rho_v}}\right) , \\ a^{lv}_{P\mu}(W) = \Lambda(W)\left(-\dfrac{\epsilon_l + \rho_l \partial_{\rho_l}(\epsilon_l)\,|_{P_l}}{m_l \partial_{P_l}(\epsilon_l)\,|_{\rho_l}} - \dfrac{\epsilon_v + \rho_v \partial_{\rho_v}(\epsilon_v)\,|_{P_v}}{m_v \partial_{P_v}(\epsilon_v)\,|_{\rho_v}}\right) \end{cases} \tag{164}$$

and:

$$\begin{cases} a^{lv}_{TP}(W) = K(W)\left(\dfrac{P_v - \rho_l^2 \partial_{\rho_l}(\epsilon_l)\,|_{T_l}}{m_l \partial_{T_l}(\epsilon_l)\,|_{\rho_l}} + \dfrac{P_v - \rho_v^2 \partial_{\rho_v}(\epsilon_v)\,|_{T_v}}{m_v \partial_{T_v}(\epsilon_v)\,|_{\rho_v}}\right) , \\ a^{lv}_{TT}(W) = q(W)\left(\dfrac{1}{m_l \partial_{T_l}(\epsilon_l)\,|_{\rho_l}} + \dfrac{1}{m_v \partial_{T_v}(\epsilon_v)\,|_{\rho_v}}\right) , \\ a^{lv}_{T\mu}(W) = \Lambda(W)\left(\dfrac{-\epsilon_l - \rho_l \partial_{\rho_l}(\epsilon_l)\,|_{T_l}}{m_l \partial_{T_l}(\epsilon_l)\,|_{\rho_l}} + \dfrac{-\epsilon_v - \rho_v \partial_{\rho_v}(\epsilon_v)\,|_{T_v}}{m_v \partial_{T_v}(\epsilon_v)\,|_{\rho_v}}\right) \end{cases} \tag{165}$$

Eventually, setting:

$$F_k = \left(\frac{1}{\rho_k \partial_{P_k}(\epsilon_k)\,|_{\rho_k}} - \frac{h_k}{T_k \partial_{T_k}(\epsilon_k)\,|_{\rho_k}}\right) \tag{166}$$

$$G_k = \frac{h_k}{T_k \partial_{T_k}(\epsilon_k)\,|_{\rho_k}}(\epsilon_k + \rho_k \partial_{\rho_k}(\epsilon_k)\,|_{T_k}) - \frac{1}{\rho_k \partial_{P_k}(\epsilon_k)\,|_{\rho_k}}(\epsilon_k + \rho_k \partial_{\rho_k}(\epsilon_k)\,|_{P_k}) \tag{167}$$

$$H_k = \frac{h_k}{T_k \partial_{T_k}(\epsilon_k)\,|_{\rho_k}}(-P_g + \rho_k^2 \partial_{\rho_k}(\epsilon_k)\,|_{T_k}) - \frac{1}{\rho_k \partial_{P_k}(\epsilon_k)\,|_{\rho_k}}(-P_g + \rho_k^2 \partial_{\rho_k}(\epsilon_k)\,|_{P_k}) \tag{168}$$

for $k = l, v$, we have:

$$\begin{cases} a^{lv}_{\mu P}(W) = K(W)\left(\dfrac{H_l}{m_l T_l} + \dfrac{H_v}{m_v T_v}\right) , \\ a^{lv}_{\mu T}(W) = q(W)\left(\dfrac{F_l}{m_l T_l} + \dfrac{F_v}{m_v T_v}\right) , \\ a^{lv}_{\mu\mu}(W) = \Lambda(W)\left(\dfrac{G_l}{m_l T_l} + \dfrac{G_v}{m_v T_v}\right) \end{cases} \tag{169}$$

The relaxation process over time is guaranteed if the three fundamentals minors are positive [42].

Appendix 6: The RIP condition

We consider the class of gas-liquid flow models discussed in section 2, thus focusing on immiscible components. We assume some initial condition $W^0(x) = W(x, t = 0)$, such that:

$$U_k(x, t = 0) = 0 \ , \tag{170}$$

and with uniform pressure and temperature fields:

$$P_k(x, t = 0) = P_0 \quad ; \quad T_k(x, t = 0) = T_0. \tag{171}$$

The flow will remain steady, if:

$$\partial_t\left(\psi\right)\left(x,t=0\right)=0 \tag{172}$$

whatever ψ is.

Obviously, the source terms vanish, and we get:

$$\begin{cases} \partial_t\left(\alpha_k\right)\left(x,t=0\right)=0\ ; \\ \partial_t\left(m_k\right)\left(x,t=0\right)=0\ ; \\ \partial_t\left(m_k U_k\right)\left(x,t=0\right)+P_0\nabla\alpha_k^0-\Pi_I(W^0)\nabla\alpha_k^0=0\ ; \\ \partial_t\left(\alpha_k E_k\right)\left(x,t=0\right)=0\ . \end{cases} \tag{173}$$

Thus the flow will remain steady if:

$$\left(P_0-\Pi_I(W^0)\right)\nabla\alpha_l^0=0 \tag{174}$$

whatever the initial profile of α_l^0 is, or in other words:

$$\Pi_I(W^0)=P_0 \tag{175}$$

This will be called the Realizable Interfacial Pressure (RIP) condition.

Appendix 7: Behaviour of the fractional step and coupled approaches when $\frac{\tau_P}{\tau_T}$ tends to zero

In this **Appendix**, the temperature relaxation time scale is set to: $\tau_T=10^{-3}s$. **Figures** 25, 26, 27 show the L^1 norm of the error on the pressure P_l, at $t=0.001s$ in case 1 (see **Appendix** 1 for details on initial data and EOS coefficients). **Figure** 27 highlights that the ratio of errors between the two methods, for a given time step, is greater than 100, within a very wide range of time steps. This ratio of errors decreases when $\frac{\tau_P}{\tau_T}=1$, see **Figure** 25, but it is still in favour of the coupled approach.

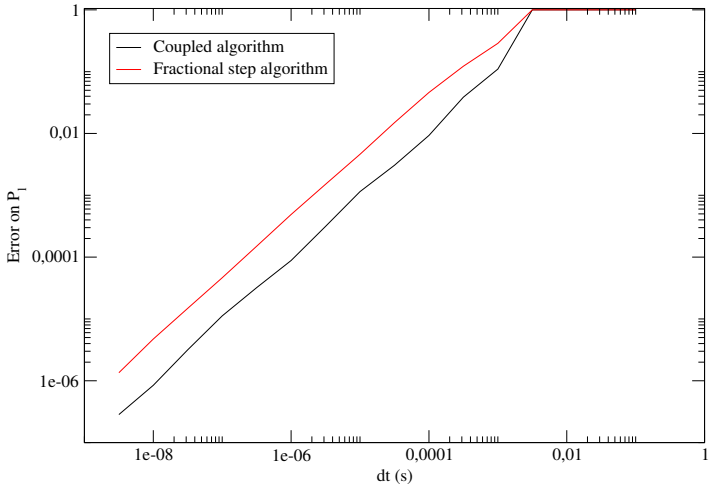

Figure 25: Convergence curve in case 1 with $\frac{\tau_P}{\tau_T}=1$.

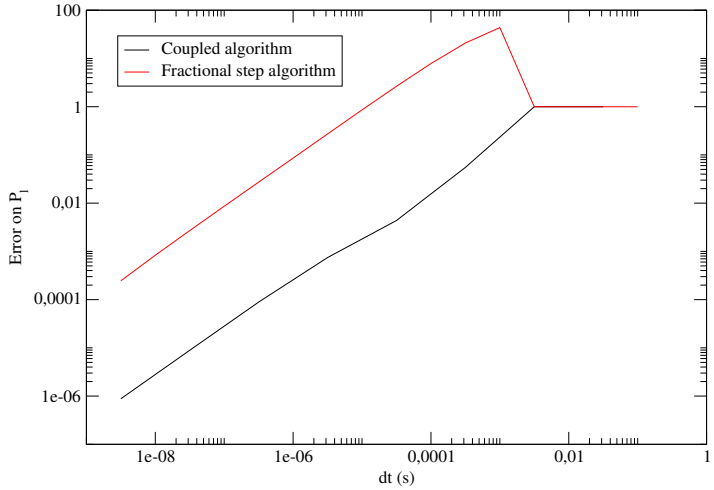

Figure 26: Convergence curve in case 1 with $\frac{\tau_P}{\tau_T} = 10^{-4}$.

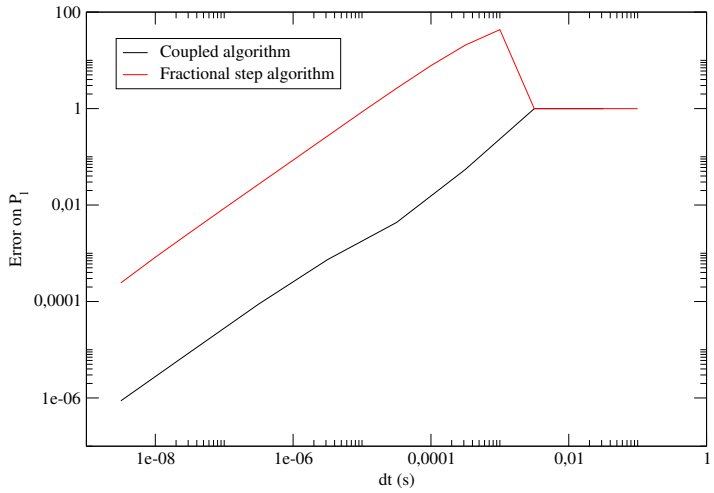

Figure 27: Convergence curve in case 1 with $\frac{\tau_P}{\tau_T} = 10^{-6}$.

Appendix 8: Chauvin experiment [12] simulated with rigid particles.

Here, Chauvin experiment [12] is simulated with rigid particles assuming constant interfacial area, associated with constant particle diameter: $D_d = 500\mu m$. The initial conditions and thermodynamic coefficients are recalled in **Appendix** 1. The relaxation time scales are the same as those used in section 2.1.3.

We recall that for collapsible droplets, as in the experiment, a pressure drop occurs right after the incident shock wave, as expected when droplet atomization arises, see [31]. The simulation captures this phenomenon quite well, see **Figure** 10.

On the other hand, **Figure** 28 shows that with rigid particles, the simulation exhibits a slow increase of the total pressure after the incident shock wave. Similar results have already been exhibited in [11] and [6].

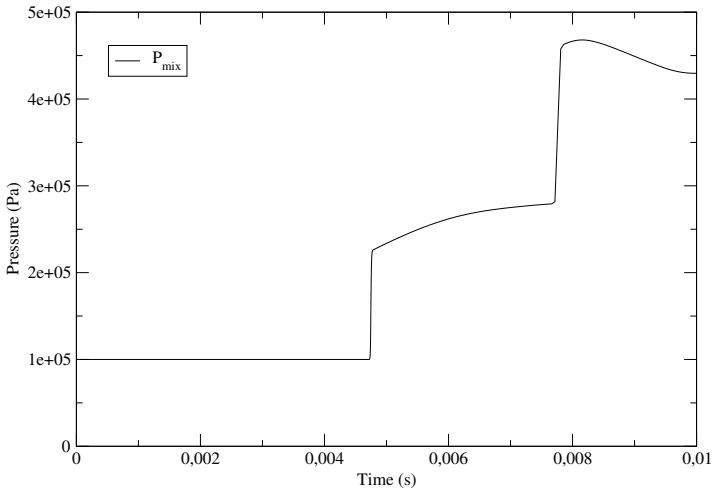

Figure 28: Chauvin experiment [12] with rigid particles of diameter $D_d = 500\mu m$. Evolution of P_{mix} at station 3 using a 10 000 cells mesh and the coupled algorithm.